RAMAN SCATTERING

IN

SILVER INTERCALATED TITANIUM DISULPHIDE

by

Richard Leonelli

B. Sc., Université de Montréal, 1977

A THESIS SUBMITTED IN PARTIAL FULFILLMENT OF

THE REQUIREMENTS FOR THE DEGREE OF

MASTER OF SCIENCE

in the Department

of

Physics

SIMON FRASER UNIVERSITY

APRIL 1980

APPROVAL

Name: Richard Lecnelli

Degree: Master of Science

Title of Thesis: Raman Scattering in
Silver Intercalated Titanium Disulphide

Examining Committee:

Chairperson: M. Plischke

J. C. Irwin
Senior Supervisor

R. F. Frindt

K. E. Rieckhoff

A. S. Barker, Jr.
External Examiner
Bell Telephone Laboratories
Visiting Professor
Department of Physics
Simon Fraser University

Date Approved: April 11, 1980

PARTIAL COPYRIGHT LICENSE

I hereby grant to Simon Fraser University the right to lend my thesis or dissertation (the title of which is shown below) to users of the Simon Fraser University Library, and to make partial or single copies only for such users or in response to a request from the library of any other university, or other educational institution, on its own behalf or for one of its users. I further agree that permission for multiple copying of this thesis for scholarly purposes may be granted by me or the Dean of Graduate Studies. It is understood that copying or publication of this thesis for financial gain shall not be allowed without my written permission.

Title of Thesis/Dissertation:

Raman Scattering in Silver Intercalated Titanium Disulphide

Author: _____

(signature)

Richard Leonelli

(name)

April 17, 1980

(date)

ABSTRACT

The ternary compound Ag_xTiS_2 has been obtained by electrochemically intercalating silver into single crystals of TiS_2. Raman scattering has been carried out on several crystals with compositions x= 0,19, 0,33, 0,41 and 0,65. The spectra obtained at low temperatures from the intercalated compounds exhibited several features not present in the ones from pure TiS_2. In the x= 0,33 compound, three additional peaks were identified and their measured energies were 128, 270 and 304 cm^{-1}. The same peaks were found in the x= 0,19 system while only the low frequency peak was observed in the x > 0,40 cases. Also, electron microscopy studies have revealed that a $\sqrt{3}a$ triangular superlattice is formed in the 0,19 and 0,33 systems at low enough temperature (T < 250 K).

The lattice dynamics of the x= 1/3 system have been investigated within a valence force field model using first a C_{3i}^2 crystal space group where the silver ions are ordered on sites of octahedral symmetry and second a C_3^4 crystal space group where the ions are on sites of tetrahedral symmetry. The number and energies of the observed peaks were satisfactorily reproduced by the analysis of the C_{3i}^2 configuration with a three parameter model. Therefore, the additional Raman features can be attributed to a zone-folding mechanism.

Raman spectra have also been obtained as a function of

temperature. The intensity dependence of the additional features has led to the identification of an order-disorder phase transition with $T_c \simeq 300$ K, in agreement with the predictions of a phase diagram obtained using a two-dimensional lattice gas model on a triangular lattice.

ACKNOWLEDGEMENTS

I would like to thank Dr. R. F. Frindt and the members of his group, P. Joensen and G. Scholz, for supplying the TiS_2 crystals and for many helpful discussions, and Dr. A. E. Curzon, for performing the electron diffraction work. I am indebted to Dr. Mike Plischke, for his patient explanations regarding the physics of critical phenomena. I would also like to mention the members of the group of Dr. Haering, from the University of British Columbia, for their collaboration.

Many special thanks to Robert Audas and Bill McMullan. I deeply appreciated their help and friendship. And, the last but not the least, I thank Dr. J. C. Irwin, for the great time I had working under his supervision.

The financial support of the citizens of Canada, through a scholarship from the Natural Sciences and Engineering Research Council, is gratefully acknowledged.

TABLE OF CONTENTS

LIST OF TABLES

LIST OF FIGURES

I. Introduction

There has been considerable interest in recent years on the subject of fast ion transport in solids. This is because of the many possible applications in the field of energy storage and also because there are many yet imperfectly understood physical phenomena involved: phase transitions, the hopping mechanism, paired and single-ion vibrations.[1]

Some of the materials exhibiting fast ion transport could serve as solid electrolytes. One can mention here silver compounds like AgI or $RbAg_4I_5$ in which, above the critical temperature, the silver atoms become mobile inside the structure formed by the iodine atoms.

Others could serve as solid electrodes. When those materials are immersed in a suitable electrolyte, a reversible topochemical reaction takes place in which ions in the solution migrate inside the electrode. The emf associated with such a reaction can be as high as several volts. In this second category one finds many transition metal dichalcogenides and, in particular, TiS_2.

Most of the transition metal dichalcogenides are part of a large and interesting family of layered compounds, that is compounds formed by the superposition of thin layers with the

---

[1] For a review, see Fast Ion Transport in Solids: Electrodes and Electrolytes

interlayer forces much smaller than the intralayer forces. It turns out that many ions can intercalate and diffuse between the layers and hence form a nearly two-dimensional fluid (Whittingham, 1978).

One way to investigate the dynamics of the mobile ions is by means of Raman scattering. Such a technique has been extensively used to probe the diffusive and oscillatory parts of the ionic motion in superionic conductors (Burns et al., 1977, Gallagher and Klein, 1979). It has also been used to study the lattice dynamics of intercalated layered compounds (Nemanich et al., 1977, Unger et al., 1979). In particular, the Raman spectra of intercalated graphite have been analysed both in terms of a zone-folding mechanism (Dresselhaus et al., 1977) and in terms of disorder-induced scattering (Caswell and Solin, 1978).

This work reports Raman scattering experiments performed on the system Ag_xTiS_2. It is an extension of previous investigations done at Simon Fraser University which revealed extra features in the Raman Spectra of Ag-intercalated TiS_2 together with the formation of a superlattice (Unger et al., 1979). But the problem of the relation between those two phenomena was left open. This work has, to some extent, elucidated that problem.

This thesis is structured in the following way. In Chapter II, the structural and chemical aspects of the Ag_xTiS_2 system are described. In Chapter III, the theory of the Raman effect in solids is reviewed and Raman selection rules are established for

two possible configurations of the $Ag_{1/3}TiS_2$ compound. Chapter IV treats the experimental aspects of the research and in Chapter V, the experimental results are analysed according to two simple models. Chapter VI presents the conclusions and suggests some further work.

II- The Ag_xTiS_2 System

2.1- Titanium Disulphide

Titanium disulphide crystallizes in the trigonal CdI_2 structure (space group D^3_{3d}) with one formula unit per cell and a hexagonal Bravais lattice (Wilson and Yoffe, 1969). It is made of two-dimensional planes of S-Ti-S units separated from each other by a "Van der Waals" gap. The titanium atoms are sandwiched between planes of sulphur and the stacks are arranged so that each Ti site lies above another Ti site in the adjacent stack. The sulphur atoms are ordered in near octahedral sixfold coordination around the Ti site within each sandwich (see Fig. 2.1).

The primitive lattice vectors in this structure can be taken as:

$$\underline{a} = \frac{1}{2}(\sqrt{3}\hat{x} - \hat{y})a \qquad (1)$$

$$\underline{b} = a\hat{y} \qquad (2)$$

$$\underline{c} = c\hat{z} \qquad (3)$$

The atomic positions in the unit cell are given by Ti: (0,0,0) and S: (1/3,2/3,u), (2/3,1/3,-u), where the parameter u

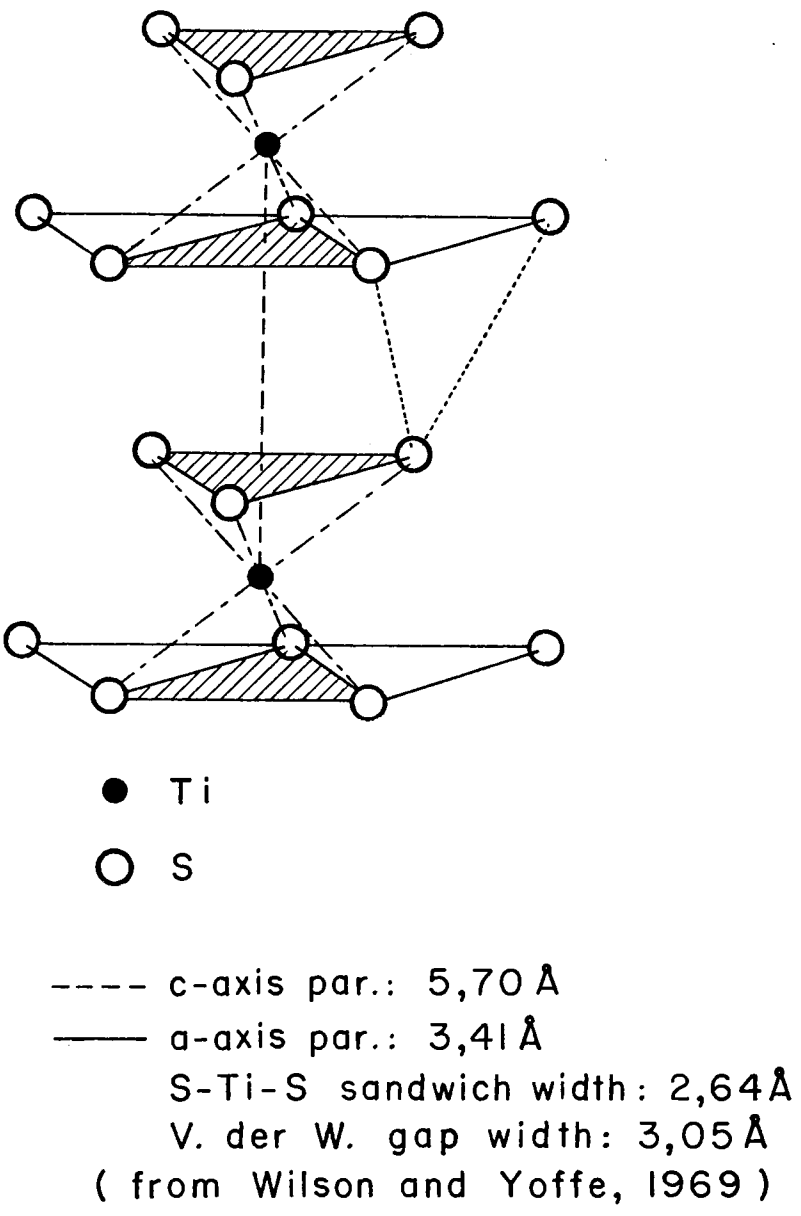

Figure 2.1- TiS_2 crystal structure.

is close to the ideal octahedral value of 1/4 (Wyckoff, 1965).

Titanium disulphide is usually a metal rich compound. The lattice parameters depend somewhat on the excess metal and have the following values for the stoichiometric compound (Thompson et al., 1975):

a= 3,3407±0,0002 Å

c= 5,6953±0,0002 Å

Optical experiments have suggested that TiS_2 is a semiconductor (Greenaway and Nitsche, 1965, Beal et al., 1972) but temperature-dependent resistivity measurements on high purity stoichiometric samples exhibited a semimetallic behaviour (Thompson et al., 1972) and an electrical resistivity approximately proportionnal to T^2 between 10 and 400 K (Thompson, 1975).

These conflicting observations can be reconciled by assuming that TiS_2 is a "dirty semiconductor". This means that even in the stoichiometric case a certain proportion of the titanium atoms are not in their usual location but are transferred into vacant interlayer sites. Only 0,4% of the titanium atoms would have to be displaced in order to explain the free carrier density of $3x10^{20}$ cm^{-3} (Wilson, 1978).

Band structure calculations indicate that TiS_2 has a very small indirect band gap (of the order of 0,2-0,3 eV) separating

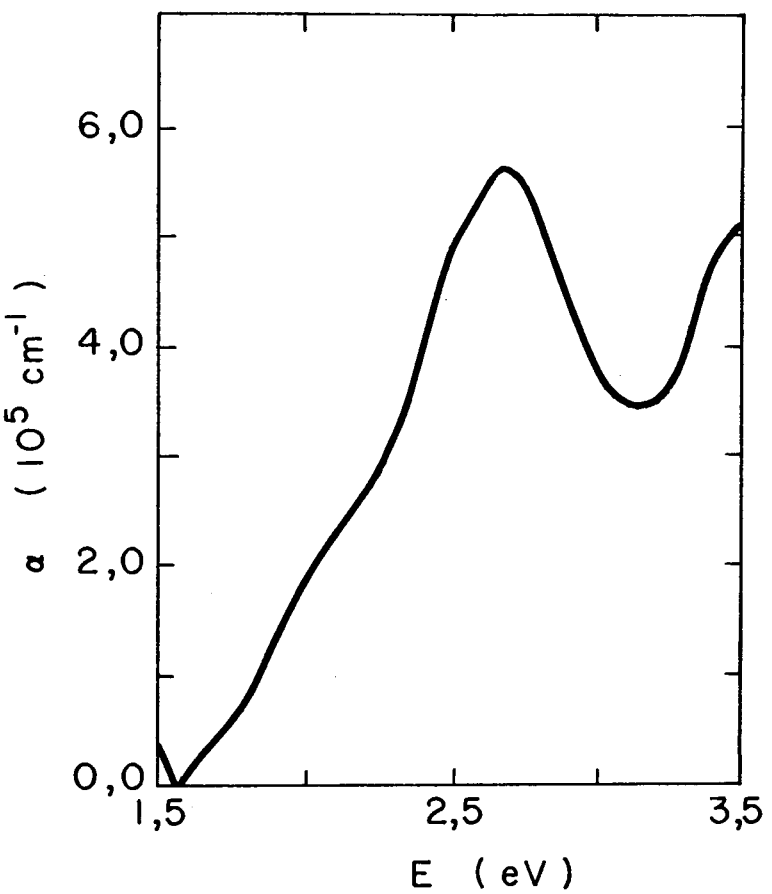

Figure 2.2- Optical absorption coefficient of TiS_2 (Beal et al., 1972).

the unoccupied d-based bands from the valence σ bands. The bonding mechanism is predominantly covalent with some minor ionic character and involves a metal s, p to nonmetal s, p chemical bond (Zunger and Freeman, 1977).

2.2- The Ag-Intercalated System: Chemical Aspects

TiS_2, like several other layered compounds, can accomodate extra atoms in its Van der Waals gap, without having its original intralayer structure changed. Compounds of the type M_xTiS_2 can be grown by iodine vapor transport for M= Cu, Ni, Fe, Co or can be obtained by an electrointercalation reaction according to

$$M^+ + TiS_2 + e^- \longrightarrow MTiS_2 + E$$

for M= Ag, Cu and several alkali metals (E is a free energy).[1]

It is useful to introduce a chemical potential μ, related to thermodynamic functions by the equation

$$dG = -SdT + Vdp - \bar{\mu}dN \qquad (4)$$

where G is the Gibbs free energy and $\bar{\mu}$ is called the electrochemical potential (Conway, 1965). The latter corresponds to the change in energy of a charged particle when it is brought from infinity to a point inside the considered electrode. It can be separated into three terms (see Fig. 2.3a):

[1] For a review, see Whittingham (1978).

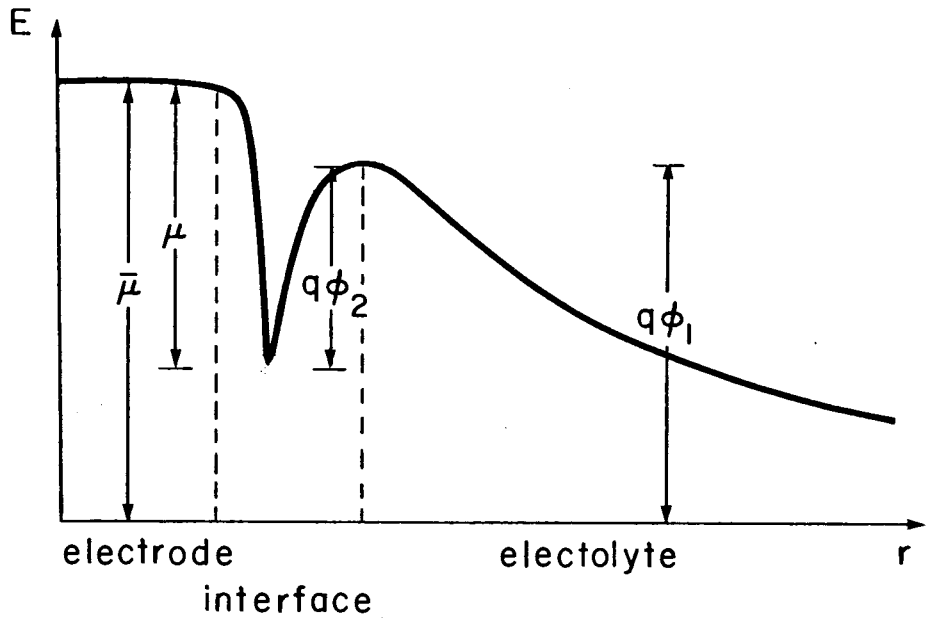

a

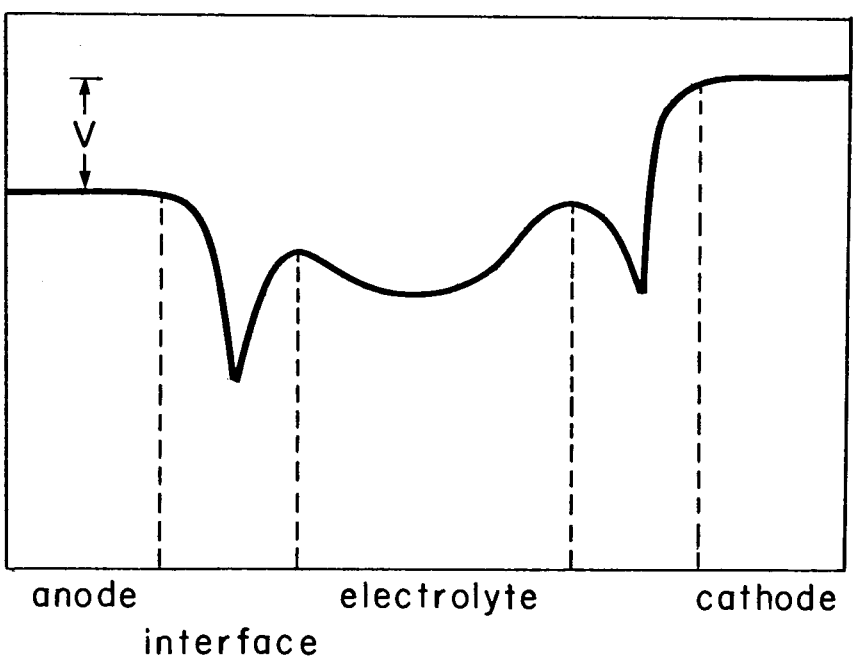

b

Figure 2.3- Electrolytic systems. a) Schematic representation of $\bar{\mu}$. b) Schematic representation of the potential between two electrodes.

a. the chemical potential μ itself, arising from interactions with the other intercalated particles and the host structure

b. an electrical term ϕ_1 coming from the interaction between the particle and any net electric field

c. a surface term ϕ_2 associated with the crossing of the surface layers,

so that one can write:

$$\bar{\mu} = \mu + q(\phi_1 - \phi_2) \qquad (5)$$

In an actual cell, the measured potential V corresponds to the difference in energy between the two electrodes (see Fig. 2.3b). If it is assumed that any change in ϕ_1 or ϕ_2 with composition can be neglected then μ is related to V by:

$$\mu = -eV + C \qquad (6)$$

where C is a constant.

2.3- The Ag-Intercalated System: Structural Aspects

Once it is inside the host structure, the intercalated ion diffuses more or less rapidly in the Van der Waals gap, as is evidenced from the observation of the intercalation process on single crystals. Fronts are seen to develop from the edges and from imperfections on the surfaces of the crystal (see Section 4.1).

In between the TiS_2 layers, the ion can occupy either octahedral or tetrahedral sites (the name of the site refers to the coordination of the sulphur atoms around it). The octahedral sites form a triangular array. The tetrahedral sites can be separated in two subsets, one set slightly above and the other one below the plane of the octahedral sites. Each of these subsets also forms a triangular array while the combination of the two is a honeycomb array whose centers correspond to the octahedral sites.

Most of the systems thus formed exhibit different phases. They correspond to:

a. n-staging, in which the intercalated species occupies 1 out of n layers of the host sructure;

b. some changes of the host sructure, usually a slippage of the initial S-Ti-S layers with respect to each other;

c. the formation of a superlattice by the intercalated species.

The changes that occur on the passage from one phase to another are expected to be observable by many different means of investigation. X-ray scattering and electrochemical measurements have been performed on silver intercalated TiS_2 in powder form by Bottini et al. (1979) (see Fig. 2.4). These measurements revealed what might be a structural change occurring at around x= 0,25.

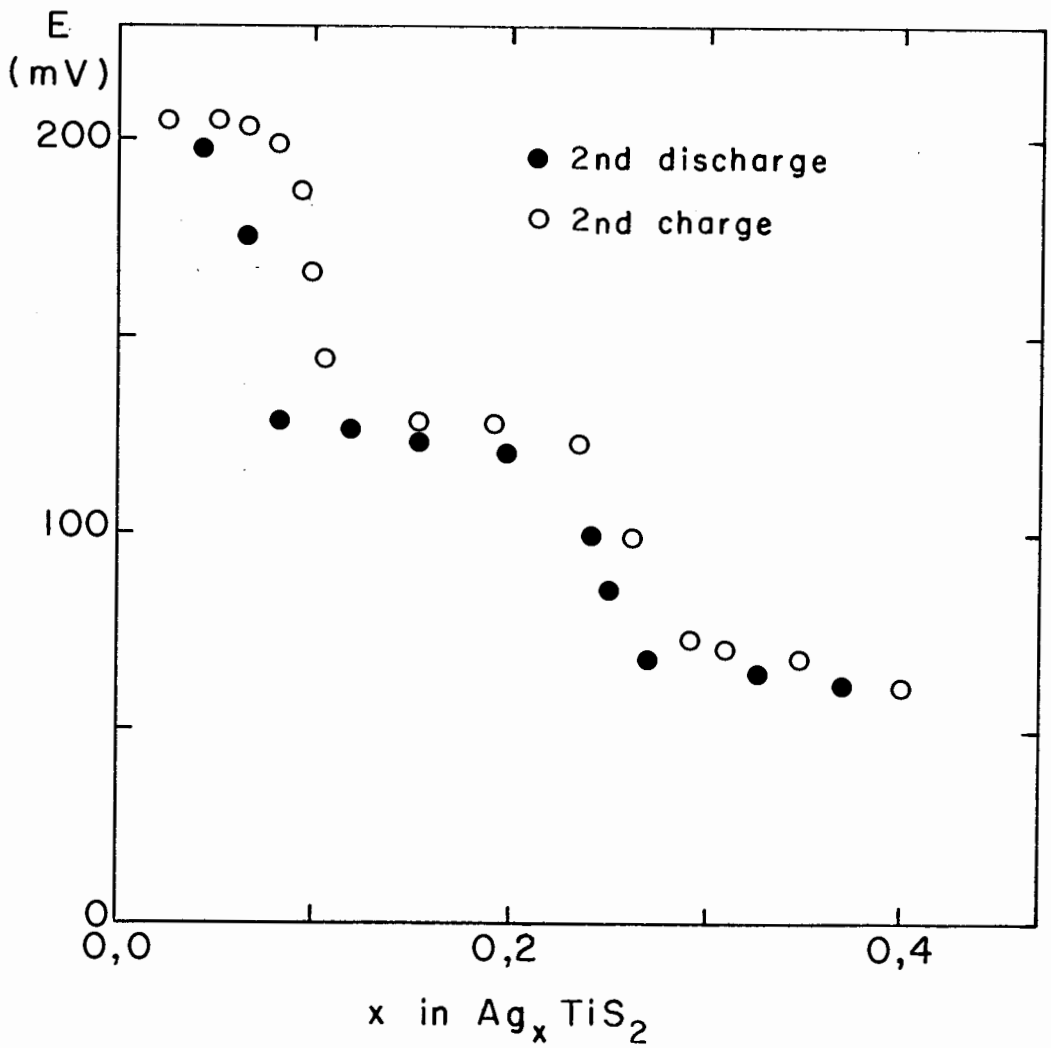

Figure 2.4- Ag_xTiS_2 cell potential as a function of the composition x (T= 100°C) (from Bottini et al., 1979).

Also, small crystals of Ag_xTiS_2 have been studied by means of electron diffraction and Raman scattering by Unger et al. (1979). The electron diffraction revealed new spots corresponding to a superlattice with lattice parameters $a' = \sqrt{3}a$ rotated by 30^0 with respect to the original lattice spots. The superlattice spots were quite bright at liquid nitrogen temperature but barely visible at room temperature.

The Raman spectra revealed new peaks, which were attributed to the superlattice formation. Although no sharp phase transition was observed, the extra peaks were seen to disappear at temperatures above 400 K.

The electron diffraction patterns are a strong indication that the silver ions order by occupying one out of three equivalent sites on a triangular lattice (see Fig. 2.5). But no complete structural study has as yet revealed if the sites in question are of octahedral or tetrahedral coordination. One thus has to look at similar systems in order to pinpoint the most probable structural arrangement.

One of the similar compounds is $AgCrS_2$. It has a rhombohedral structure ($R\bar{3}m$) in which the sulfur atoms assume an octahedral coordination around the chromium atom and a tetrahedral one around the silver atoms. Two phases are observed. In the low temperature phase, the silver atoms are ordered on one of the two subsets of tetrahedral sites while in the high temperature phase they are randomly distributed over both type

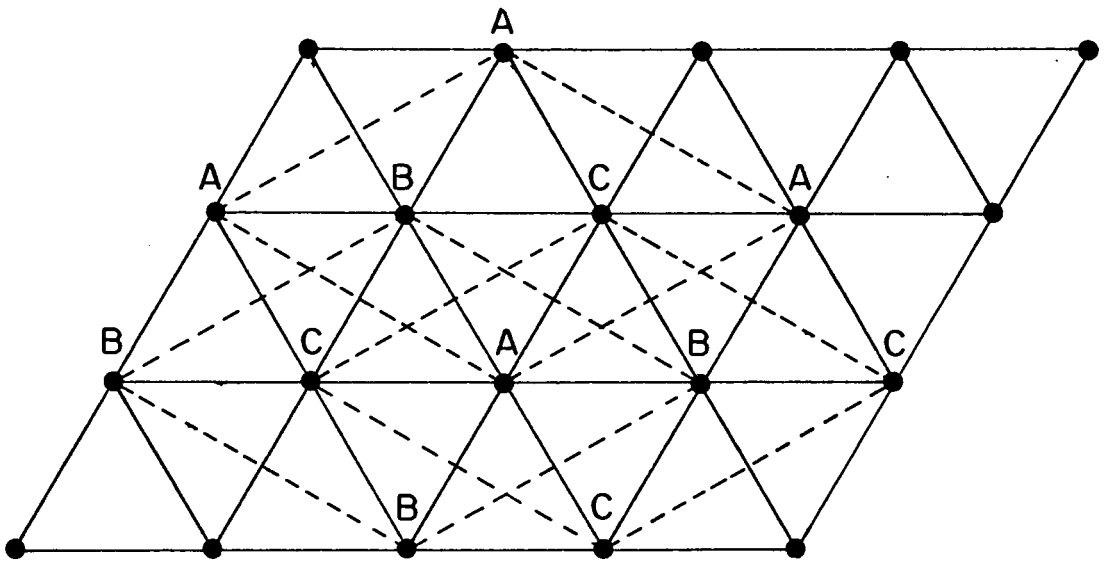

Figure 2.5- Triangular lattice. Dashed lines: A, B and C sublattices.

of sites (Engelsman et al., 1973).

It is also observed that silver occupies tetrahedral sites in TaS_2 although a complete structural analysis with composition and temperature has not been carried out yet.[2]

It is expected that silver atoms would behave somewhat similarly to Cu atoms since they have the same electronic configuration. Copper has been intercalated in several layered compounds. In Cu_xTiS_2, for values of x greater than 0,7, the copper atoms occupy tetrahedral sites and the TiS_2 layers translate to form a rhombohedral structure derived from 3 initial TiS_2 cells (LeNagard et al., 1975). Cu-intercalated TiS_2 also exists in a more complex spinel structure $Cu_{1-x}\ Ti_2S_4$ with x between 0 and 0,44 (LeNagard et al., 1975b).

It is also interesting to look at the case of Cu_xNbS_2. Like TaS_2, NbS_2 has a 2H structure (space group D^4_{6h}). Upon intercalation with copper, the NbS_2 planes slip so that their structure goes from the 2H-NbS_2 type to the 2H-MoS_2 type. The copper atoms occupy the tetrahedral sites and are found to order at compositions of x=0,0625, 0,25, 0,33 and 0,5 if the temperature is low enough (Boswell et al., 1976).

At x=0,0625, the copper atoms occupy 1/16th of the available sites of one of the two sets of tetrahedral sites while at x=0,25, it occupies 1 out of 4 of those sites and forms a triangular superlattice with parameter a'= 2a if the

[2] G. Scholz, private communication.

temperature is below 410 K. At x= 0,33, the 2a superlattice is again seen at temperatures below 410 K while a 4a superlattice appears at temperatures lower than 180 K. Thus, the case x=0,33 consists in a combination of ordering at x=0,25 on one subset and x=0,0625 on the other. At x=0,50, the copper atoms order in a 2a superlattice on both subsets of tetrahedral sites for T < 230 K. No ordered structure has been observed at x=0,67.

On the other hand, TiS_2 has been intercalated by other metals such as Ni and Fe, although not electrochemically (Danot et al., 1972, Takahashi and Yamada, 1973). In both cases, the interstitial atoms were seen to occupy octahedral sites and an ordered structure for x=1/3 was observed, without any slippage of the TiS_2 planes. The Fe and Ni cases differed in that the ordering along the c axis was found to be different. The structural arrangement of the Fe atoms reproduced itself every two layers while the Ni arrangement had a periodicity of three layers.

From all that precedes, some broad conclusions can be drawn. First, although the silver is expected to have a natural tendency to sit in tetrahedral sites, the more spacious octahedral sites cannot be ruled out at low concentrations. Second, a slippage of the TiS_2 planes is possible but not necessary to accomodate the interstitial atoms. Finally, the silver atoms are expected to order in a triangular superlattice on either the octahedral or the tetrahedral sites.

2.3- The Lattice Gas Model

The study of an eventual order-disorder phase transition in intercalated TiS_2 is very interesting in itself given the recent developments in the theory of phase transitions due to the renormalization group method.

In particular, the behaviour of an intercalated species can be modeled in a simple way by the lattice gas model, in which the particles are constrained to reside on lattice sites. A suitable Hamiltonian is:

$$H = \sum_{<ij>} U_{ij} n_i n_j - \mu \sum_i n_i \qquad (7)$$

where the indices i and j run over the lattice points and n_i is 1 if the ith site is occupied and 0 if not. The notation "<ij>" refers here to all pairs of sites counted once.

The first term represents the interaction between pairs of particles and the second the energy required to "create" a new particle in the lattice.

The interaction between pairs of ions is expected to fall off rapidly with distance due to the screening from the delocalized electrons in the lattice. Moreover, given the geometry of the host lattice, the in-plane interactions should be much stronger than any silver-silver interaction along the c-axis.

It is therefore reasonable to assume that the silver ions interact as if they could occupy only the sites of a triangular lattice. In effect, such a lattice can be either formed by the octahedral sites or by one of the two subsets of tetrahedral sites.

Also, it is useful to make the following transformation:

$$n_i = \frac{1}{2}(1 + S_i), \qquad S_i = +1 \text{ or } -1 \tag{8}$$

Replacing (8) in (7), developing up to the third nearest neighbour on a triangular lattice and discarding constant terms, one gets:

$$H = \frac{1}{4} \sum_{<nn>} U_1 S_i S_j + \frac{1}{4} \sum_{<snn>} U_2 S_i S_j + \frac{1}{4} \sum_{<tnn>} U_3 S_i S_j + \frac{1}{2} \sum_i [3(U_1 + U_2 + U_3) - \mu] S_i \tag{9}$$

where nn, snn and tnn refer to the first, second and third nearest neighbour respectively (six of each kind for each lattice site), and U_1, U_2, U_3 refer to the first, second and third nearest neighbour interaction. From equation (9), one can see that the lattice gas model is actually equivalent to an Ising spin model (Huang, 1963).

A triangular lattice can be divided into three sublattices A, B and C, each site of a given sublattice having only sites of the two others as first neighbour (see Fig. 2.5). If U_1 is positive and much bigger than U_2 and U_3, it is expected that the

lattice gas will exhibit an ordered phase in which one of the sublattices is preferentially occupied or empty.

Schick et al. (1977) have treated the triangular lattice with first neighbour repulsive interaction using real-space renormalisation group techniques. Their results indicate that the lattice gas undergoes a second order phase transition.

For such a transition, it is possible to define a long range order parameter η which goes continuously from 1 in the ordered structure to 0 at the phase transition. For the triangular lattice gas, an expression satisfying the above property is:

$$\eta = x_A - \frac{1}{2}(x_B + x_C) \qquad (10)$$

where x_A is taken as being the preferentially occupied or empty sublattice.

The phase diagram obtained by Schick et al. is depicted in Figure 2.6. It shows that an ordered $\sqrt{3}a$ structure can exist only for fairly narrow spans of the composition x centered around 0,33 and 0,67.

The above model does not preclude the possibility of an ordering along the c-axis. For example, in several antiferromagnets where the in-plane interactions are much stronger than the out-of-plane interactions, the phase transition has a two-dimensional character except very near the critical point. Yet, at the phase transition, a tridimensional ordering is

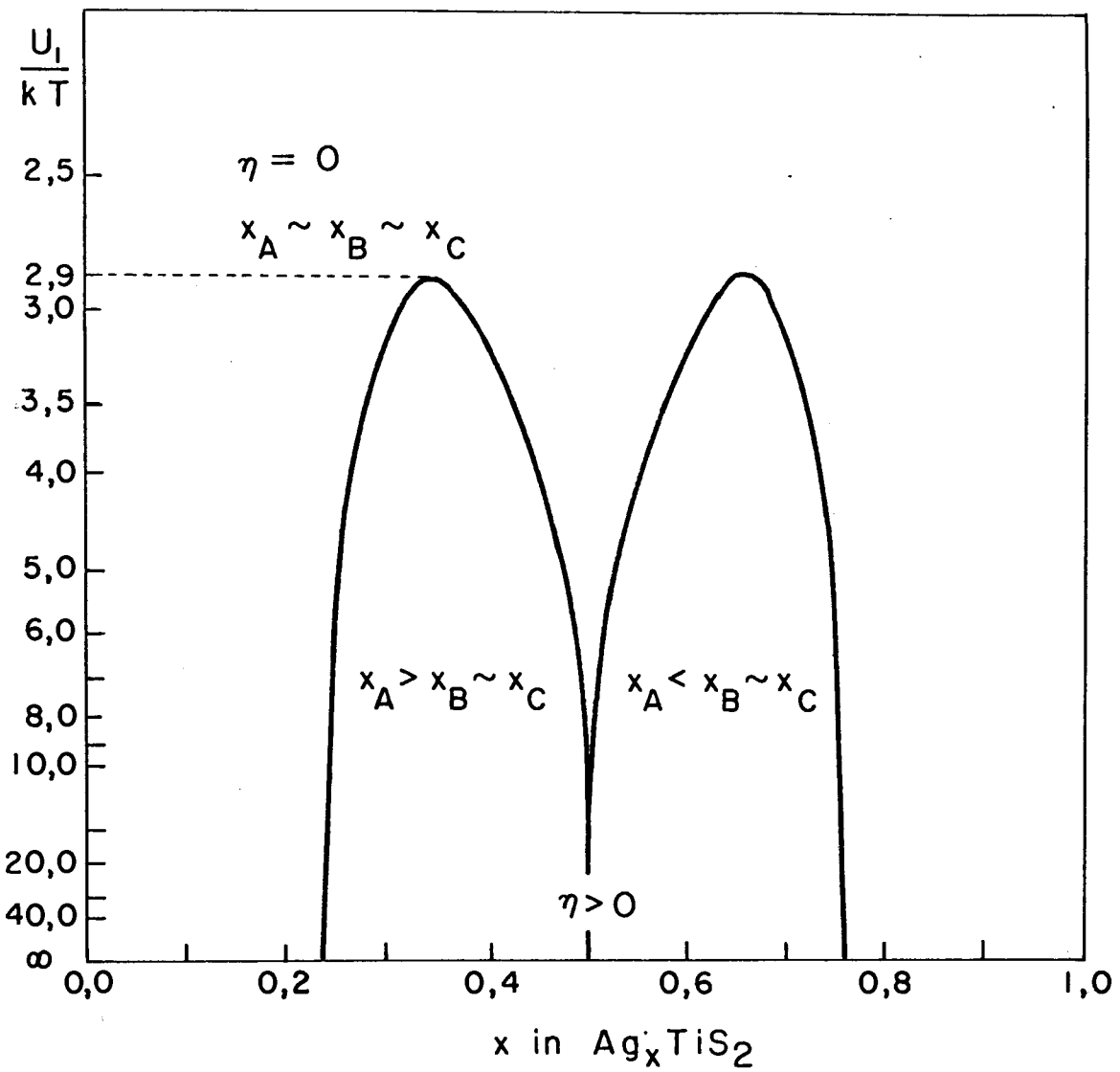

Figure 2.6- Phase diagram for a bidimensional triangular lattice gas with only first neighbour interaction.

achieved (Birgeneau et al., 1973). Along the same lines, it is expected that in Ag_xTiS_2, the silver 'gas' would have a two-dimensional character and that at the disorder-order transition, the different planes of silver atoms would rearrange themselves in the most favourable configuration.

III. The Raman Effect

A. Theory of the Raman Effect in Crystals

3.1- Crystal Dynamics

A crystal can be assumed to be made of a large number N of primitive cells, each containing an s atom basis.

Let $\underline{x}(mj)$ be the position of the jth atom in the mth cell and

$$\underline{u}(mj) = \underline{x}(mj) - \underline{x}_0(mj) \qquad (1)$$

be its displacement from equilibrium position caused by thermal fluctuations. In the harmonic approximation, the potential function of the lattice is developed to second order in terms of the atomic displacements so that the Hamiltonian can be written as[1]:

---

[1]For a more detailed discussion, see Poulet and Mathieu (1970) or Maradudin et al. (1971).

$$H = \frac{1}{2} \sum_{mj\alpha} M_j \dot{u}_\alpha^2(mj) + \Phi_0 + \frac{1}{2} \sum_{mj\alpha} \sum_{m'j'\beta} \phi_{\alpha\beta}(mj,m'j') u_\alpha(mj) u_\beta(m'j') \quad (2)$$

where M_j is the mass of the jth atom.

The equations of motion follow from (2):

$$M_j \ddot{u}_\alpha(mj) = - \sum_{m'j'\beta} \phi_{\alpha\beta}(mj,m'j') u_\beta(m'j') \quad (3)$$

Seeking solutions to those equations of the form:

$$u_\alpha(mj) = M_j^{-\frac{1}{2}} u_\alpha(j) e^{-i\omega t + i\underline{k}\cdot\underline{x}(m)} \quad (4)$$

one gets:

$$\omega^2 u_\alpha(j) = \sum_{j'\beta} F_{\alpha\beta}(jj',\underline{k}) u_\beta(j') \quad (5)$$

where $F_{\alpha\beta}$ is the Fourier transform of $\phi_{\alpha\beta}$:

$$F_{\alpha\beta}(jj',\underline{k}) = (M_j M_{j'})^{-\frac{1}{2}} \sum_{m'} \phi_{\alpha\beta}(mj,m'j') e^{-i\underline{k}\cdot[\underline{x}(m) - \underline{x}(m')]} \quad (6)$$

The matrix $[F(\underline{k})]$ is called the dynamical matrix. Its 3s eigenvectors $d_r(\underline{k})$ describe the oscillations of the different atoms of the cell in the vibrationnal mode r while its eigenvalues are the sqare of the characteristic frequencies $\omega_r(\underline{k})$ (r runs over the 3s degrees of freedom for each $\underline{k}$).

Because the Hamiltonian is the sum of two quadratic expressions, it is possible to find a system of coordinates in which the kinetic and potential energy take simultaneously a

diagonal form.

Those new coordinates Q_r, called normal coordinates, are related to the nuclear coordinates by:

$$u_\alpha(mj) = (NM_j)^{-\frac{1}{2}} \sum_{\underline{k},r} d_{\alpha r}(j,\underline{k}) Q_r(\underline{k}) e^{i\underline{k}\cdot\underline{x}(m)} \qquad (7)$$

Since $u_\alpha(mj)$ is real, the normal coordinates must satisfy the condition

$$Q_r(\underline{k}) = Q_r^*(-\underline{k}) \qquad (8)$$

The Hamiltonian can now be written as:

$$H = \frac{1}{2} \sum_{\underline{k},r} \left(Q_r^*(\underline{k}) Q_r(\underline{k}) + \omega_r^2(\underline{k}) Q_r^*(\underline{k}) Q_r(\underline{k}) \right) \qquad (9)$$

3.2- Symmetry of the normal coordinates

Let $(R,\underline{t})$ be a symmetry operation under which

$$\underline{k} \xrightarrow{(R,\underline{t})} \underline{k} + \underline{K}$$

where K is a reciprocal lattice vector.

All the operations $(R,\underline{t})$ form a group, $\mathcal{G}(\underline{k})$, which is a sub-group of the crystal space group $\mathcal{G}$. It can be shown (Poulet and Mathieu, 1976) that under such an operation,

$$Q_r(\underline{k}) \xrightarrow{(R,\underline{t})} Q'_r(\underline{k}) = e^{-i\underline{k}\cdot\underline{t}} \sum_{r'} D_{\underline{k}}(R)_{rr'} Q_{r'}(\underline{k}) \qquad (10)$$

where

$$D_{\underline{k}}(R)_{rr'} = \sum_{j\alpha} \sum_{j'\beta} d^{*}_{\alpha r}(j,\underline{k}) e^{-i\underline{k}\cdot\underline{x}(j)} \times R_{\alpha\beta}(j,j') d_{\beta r'}(j',\underline{k}) e^{-i\underline{k}\cdot\underline{x}(j')} \quad (11)$$

Moreover, if $Q_r(\underline{k})$ satisfies

$$Q_r(\underline{k}) + \omega_r(\underline{k}) = 0 \quad (12)$$

then so does $Q'_r(\underline{k})$.

It follows from (10) and (12) that in the system of coordinates Q_r, the matrices $[D_{\underline{k}}(R)]$ take a completely reduced form, that is they can be written as the direct sum:

$$[D_{\underline{k}}(R)] = \sum_{\ell} g^{\ell} [D^{\ell}_{\underline{k}}(R)] \quad (13)$$

Each set of degenerate coordinates satisfying the same differential equation (12) forms a basis for an irreducible representation $[D^{\ell}_{\underline{k}}(r)]$ of the crystal point group $\mathcal{G}_o(\underline{k})$ formed by all the operations R. Each representation corresponds to a normal mode of vibration of the crystal.

3.3- Phonons

In a quantum mechanical description of the lattice dynamics, the normal coordinates become operators acting on the states of the system.

The Hamiltonian (9) can be written as:

$$H = \sum_{\underline{k},r} \hbar\omega_r(\underline{k})(a^{\dagger}_{\underline{k}r}a_{\underline{k}r} + \frac{1}{2}) \tag{14}$$

The operators $a^{\dagger}_{kr}$ and a_{kr} create or annihilate a quasiparticle called a phonon. They obey the usual commutation relations

$$[a_{\underline{k}r}, a^{\dagger}_{\underline{k}'r'}] = \delta(\underline{k} - \underline{k}')\delta_{rr'} \tag{15}$$

$$[a_{\underline{k}r}, a_{\underline{k}'r'}] = [a^{\dagger}_{\underline{k}r}, a^{\dagger}_{\underline{k}'r'}] = 0 \tag{16}$$

and are related to the normal coordinate operators by:

$$Q_r(\underline{k}) = \left(\frac{\hbar}{2\omega_r(\underline{k})}\right)^{-\frac{1}{2}}(a^{\dagger}_{kr} + a_{-\underline{k}r}) \tag{17}$$

$$P_r(\underline{k}) = -i\hbar\frac{\partial}{\partial Q_r(\underline{k})} = i\left(\frac{\hbar\omega_r(\underline{k})}{2}\right)^{-\frac{1}{2}}(a^{\dagger}_{\underline{k}r} - a_{-\underline{k}r}) \tag{18}$$

3.4- Inelastic Light Scattering

The process mainly responsible for one-phonon Stokes scattering can be represented by the diagram of Figure 3.1a, with H_{EL} and H_{ER} representing the first order interaction between the electron and the lattice or the radiation. Since the process involves third order pertubation theory, a rigorous analysis is difficult but simplifying assumptions can be made if certain conditions are met.

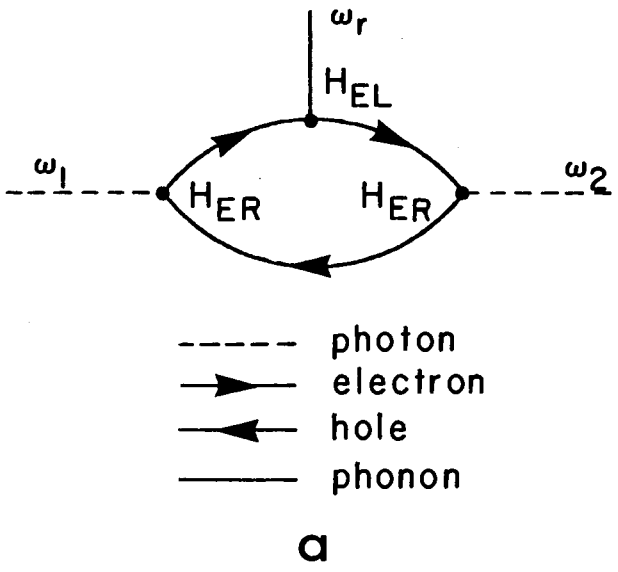

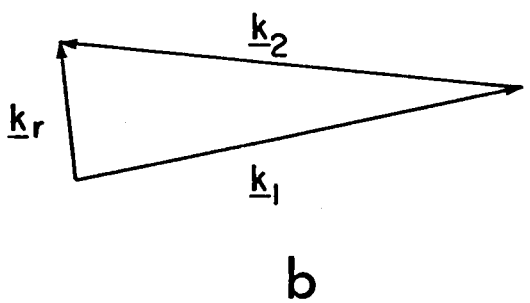

Figure 3.1- Raman scattering. a) Scattering process.
b) Scattering geometry.

First, the incident light frequency must be far from any resonances in the electronic system so that the initial and final electronic states are the same. Second, the incident light wavelength must be large compared with the interatomic distances.

The second condition enables one to assume that the scattering process involves $\underline{k}= \underline{0}$ phonons because the total momentum must be conserved (see fig 3.2b). It also allows to consider the scatterer as a Hertz dipole.

Let the incident electric field be

$$\underline{E}_1(t)= \hat{e}_1 E_{0\,1}(e^{i\omega_1 t} + e^{-i\omega_1 t}) \tag{19}$$

Classically, this field induces a dipole moment M wich reradiates energy, the scattered light intensity I_2 being:

$$I_2 R^2 d\Omega= \frac{1}{4\pi\varepsilon_0} \frac{\omega_2^4 \varepsilon_2^{\frac{1}{2}}}{2\pi c^3} (\hat{e}_2 \cdot \underline{M}) d\Omega \tag{20}$$

where ε_2 is the dielectric constant in the scattering medium and e_2 refers to the polarization of the scattered radiation.

Equation (20) can be rewritten in a semi-classical formulation as:

$$I_2(\nu \longrightarrow \nu') R^2 d\Omega= \frac{1}{4\pi\varepsilon_0} \frac{(\omega_1+\omega)^4}{2\pi c^3} \varepsilon_2^{\frac{1}{2}} |\langle \nu | \hat{e}_2 \cdot \underline{M} | \nu' \rangle|^2 \times \delta(h\omega - (E_{\nu'} - E_{\nu})) d\Omega \tag{21}$$

where the index ν refers to the lattice vibration state and the

electronic state is assumed unchanged. M is now an operator defined by:

$$\underline{M} = -\sum_j e\underline{r}_j \tag{22}$$

where the sum extends over the electronic positions.

It is convenient to define a polarisability tensor operator P by:

$$\underline{M} = P\hat{e}_1 E_{0\,1} \tag{23}$$

Replacing (23) in (21) gives:

$$I_2(\nu \longrightarrow \nu')R^2 d\Omega = \frac{1}{4\pi\varepsilon_0}\,\frac{(\omega_1+\omega)^4}{2\pi c^3}\,\varepsilon_2^{\frac{1}{2}}\,|\hat{e}_2 \cdot P^{\nu\nu'}\hat{e}_1|^2 \times E_{0\,1}^2\,(h\omega-(E_{\nu'}-E_{\nu}))\,d\Omega \tag{24}$$

with $$P^{\nu\nu'} = \langle\nu|P|\nu'\rangle$$

The polarisability tensor depends on the frequency of the incident light and on the structure of the crystal.

Explicitely one can expand P in a Taylor series:

$$P_{\alpha\beta} = P_{\alpha\beta}^{(0)} + P_{\alpha\beta}^{(1)} + \ldots \tag{25}$$

$P_{\alpha\beta}^{(0)}$ is responsible for the elastic or Rayleigh scattering and

$$P_{\alpha\beta}^{(1)} = \sum_{mj\gamma} P_{\alpha\beta,\gamma}(mj)\,u_\gamma(mj) \tag{26}$$

gives rise to one-phonon scattering.

Making use of the first simplifying assumption, it is possible to rewrite (26) in terms of the $\underline{k}= \underline{0}$ normal coordinates as:

$$P^{(1)}_{\alpha\beta} = N^{\frac{1}{2}} \sum_{r} P_{\alpha\beta}(r,\underline{0})Q_r(\underline{0}) \qquad (27)$$

where

$$P_{\alpha\beta}(r,\underline{0}) = \sum_{j\gamma} P_{\alpha\beta,\gamma}(j)M_j^{-\frac{1}{2}}d_{\gamma r}(j,\underline{0}) \qquad (28)$$

Equation (27) is invariant under a translation since only the $\underline{k}= \underline{0}$ normal coordinates are involved. Therefore, one only has to consider the effects of a symmetry operation R, an element
of the point group $\mathcal{G}_o(\underline{k})$ corresponding to the crystal space group $\mathcal{G}$.

One can do so in two ways:

a. by considering the transformations (10) undergone by the normal coordinates

b. by considering the corresponding transformation of the components of the polarisability tensor.

The fact that these two methods are equivalent results in a series of selection rules from which one can determine the form of the Raman tensors $P(r,\underline{0})$ associated with each of the Raman active normal modes of vibration of the crystal.

3.5- Anti-Stokes to Stokes scattering intensity ratio

Making use of (27), (24) can be rewritten as:

$$I_2(\nu \longrightarrow \nu') = C \sum_{\alpha\beta\alpha'\alpha'} \sum_{rr'} P_{\alpha\beta}(r,\underline{0}) P^*_{\alpha'\beta'}(r',\underline{0}) e_{1\beta} e_{1\beta'} e_{2\alpha} e_{2\alpha'} \times (\omega_1+\omega)^4 |\langle \nu | Q_r(\underline{0}) | \nu' \rangle|^2 \delta(h\omega - (E_{\nu'} - E_{\nu})) \quad (29)$$

In order to evaluate (29), one has to introduce the statistical operator ρ to describe the mixture of states representing an actual system. It is given by:

$$\rho = \frac{\exp(-H/kT)}{Tr[\exp(-K/kT)]} \quad (30)$$

The average value of an observable A is then:

$$\langle A \rangle = Tr(\rho A) \quad (31)$$

Moreover, it is useful to replace the delta function by one of its representations, namely:

$$\delta(x) = \frac{1}{2\pi} \int_{-\infty}^{\infty} e^{itx} dt \quad (32)$$

so that the total scattered intensity becomes:

$$I_2 = C' \sum_{\alpha\beta\alpha'\beta'} \sum_{rr'} P_{\alpha\beta}(r,\underline{0}) P^*_{\alpha'\beta'}(r',\underline{0}) e_{1\beta} e_{1\beta'} e_{2\alpha} e_{2\alpha'} \times \int_{-\infty}^{\infty} e^{i\omega t} (\omega_1+\omega)^4 \langle Q_r(\underline{0},t) Q_{r'}(\underline{0},0) \rangle dt \quad (33)$$

with

$$Q_r(\underline{0},t) = \left(\frac{\hbar}{2\omega_r(\underline{0})}\right) \left[a^{\dagger}_{\underline{0}r} e^{i\omega_r(\underline{0})t} + a_{\underline{0}r} e^{-i\omega_r(\underline{0})t} \right] \quad (34)$$

Replacing the expression (14) for the Hamiltonian in (30) and using the commutation relations (15) and (16), it is straightforward to show that:

$$\langle a_{\underline{k}r} a^{\dagger}_{\underline{k}'r'} \rangle = \delta(\underline{k}-\underline{k})\delta_{rr'}(n_{\underline{k}r}+1) \tag{35}$$

$$\langle a_{\underline{k}r} a_{\underline{k}'r'} \rangle = \langle a^{\dagger}_{\underline{k}r} a^{\dagger}_{\underline{k}'r'} \rangle = 0 \tag{36}$$

with

$$n_{\underline{k}r} = (e^{\hbar\omega_r(\underline{k})/kT} - 1)^{-1} \tag{37}$$

With these expressions, one gets

$$\langle Q_r(\underline{0},t) Q^{\dagger}_{r'}(\underline{0},0) \rangle = \left(\frac{\hbar}{2\omega_r(\underline{0})}\right)\left[n_{\underline{0}r} e^{i\omega_r(\underline{0})t} + (n_{\underline{0}r}+1)e^{-i\omega_r(\underline{0})t}\right] \tag{38}$$

so that

$$\begin{aligned} I_2 &= C'' \sum_{\alpha\beta\alpha'\beta'} \sum_{r} P_{\alpha\beta}(r,\underline{0}) P^{*}_{\alpha'\beta'}(r,\underline{0}) e_{1\beta} e_{1\beta'} e_{2\alpha} e_{2\alpha'} \\ &\quad \times \int_{-\infty}^{\infty} \frac{(\omega_1+\omega)^4}{\omega_r(\underline{0})} \left[n_{\underline{0}r} e^{i(\omega+\omega_r(\underline{0}))t} + (n_{\underline{0}r}+1) e^{i(\omega-\omega_r(\underline{0}))t}\right] dt \\ &= C''' \sum_{\alpha\beta\alpha'\beta'} \sum_{r} P_{\alpha\beta}(r,\underline{0}) P^{*}_{\alpha'\beta'}(r,\underline{0}) e_{1\beta} e_{1\beta'} e_{2\alpha} e_{2\alpha'} \\ &\quad \times \omega_r(\underline{0})^{-1} \left[(\omega_1+\omega_r(\underline{0}))^4 n_{\underline{0}r} + (\omega_1-\omega_r(\underline{0}))^4 (n_{\underline{0}r}+1)\right] \end{aligned} \tag{39}$$

The first term in (39) corresponds to a Stokes process in which the incident photon creates a phonon of energy $\hbar\omega_r(\underline{0})$ while the second corresponds to an anti-Stokes process in wich

the photon gains an energy $h\omega_r(0)$ by annihilating a phonon.

The intensity ratio between those two processes is easily found from (39):

$$\frac{I_{AS}}{I_S} = \left(\frac{\omega_1 + \omega_r(\underline{0})}{\omega_1 - \omega_r(\underline{0})}\right)^4 e^{-h\omega_r(\underline{0})/kT} \qquad (40)$$

B- Normal Mode Analysis of Ag_xTiS_2

3.6- Raman Selection Rules in $Ag_{1/3}TiS_2$

The ordering of silver atoms in a superlattice with lattice parameter $a' = \sqrt{3}a$ introduces a new periodicity in the structure of the crystal. This new periodicity reflects itself on the Brillouin zone and, since the superlattice is commensurate with the host lattice, a zone-folding mechanism occurs.

Such a mechanism involves the fact that the K points on the TiS_2 Brillouin zone edge become points at the center of the new Brillouin zone (see fig. 3.2). Therefore, phonons that were not Raman active in TiS_2 get "folded" onto the $\underline{k} = \underline{0}$ zone center and may become Raman active.

To predict the number and symmetry of those active modes, it is sufficient to know the irreducible representations of the point group of the new crystal sructure at the zone center Γ, as has been seen in sections 3.2 and 3.4. The possible structures

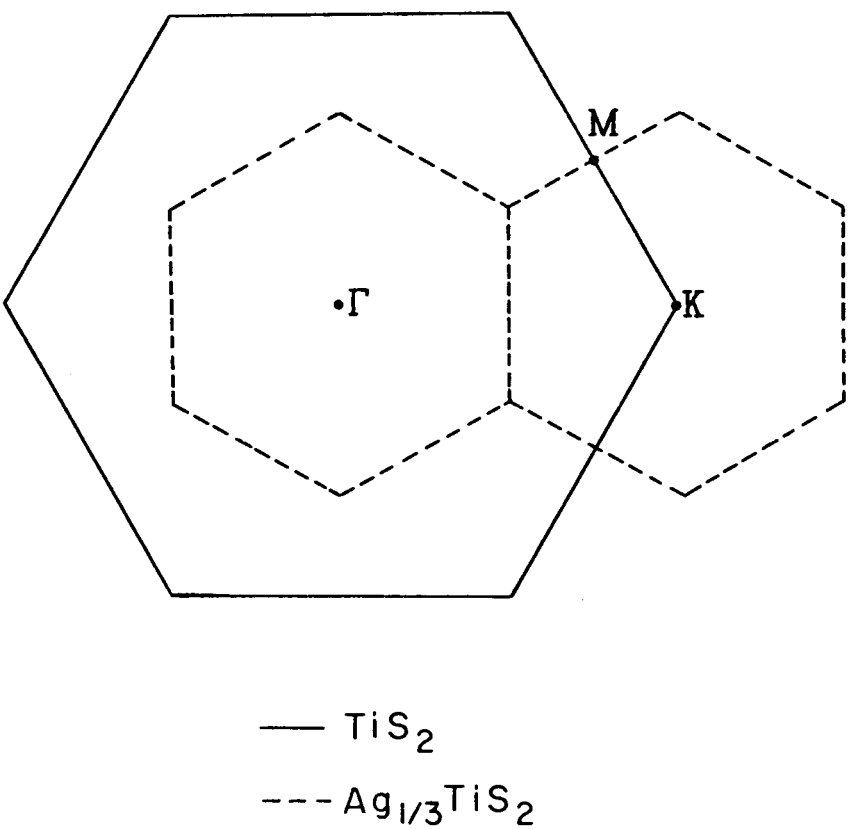

Figure 3.2- Basal plane projection of the first Brillouin zone in TiS_2 and $Ag_{1/3}TiS_2$.

of $Ag_{1/3}TiS_2$ have been discussed in section 2.3.

In the analysis found below, it was assumed that the TiS_2 layers do not slip but have the original 1T structure at least for the low x region. Also, the ABC stacking sequence was deemed more probable because it is energetically more favorable (McKinnon and Haering).

Those arguments leave two cases for further consideration:

1. 1T-TiS_2 layer structure with an ABC stacking of the silver atoms on octahedral sites (see Fig. 3.3).
2. 1T-TiS_2 layer structure with an ABC stacking sequence of the silver atoms on tetrahedral sites (see Fig. 3.4).

The pertinent space group for the first case is C_{3i}^2 (Danot et al., 1972). For the second case, the space group was obtained by an examination of the available sites in the trigonal space groups, as given in International Tables for X-Ray Crystallography (1969). It was found that the space group with the largest number of symmetry elements having enough sites to contain all the required atoms was C_3^4.

The irreducible representations of the point groups corresponding to the C_{3i}^2 and C_3^4 space groups can be obtained from the correlation method of group theory (Fateley et al., 1972). An explanation of the method and the correlation tables

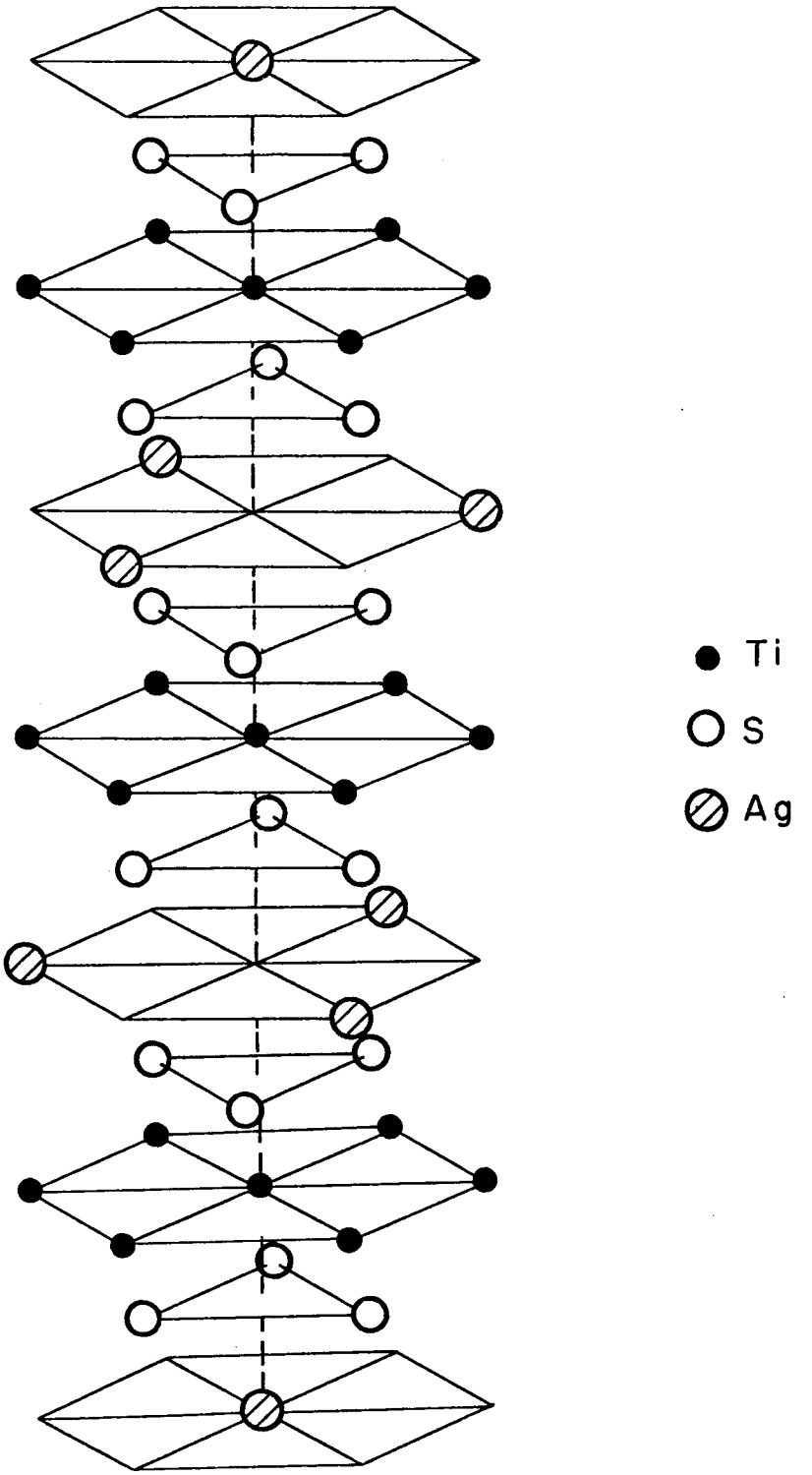

Figure 3.3- Unit cell of $Ag_{1/3}TiS_2$ in the C_{3i}^2 configuration.

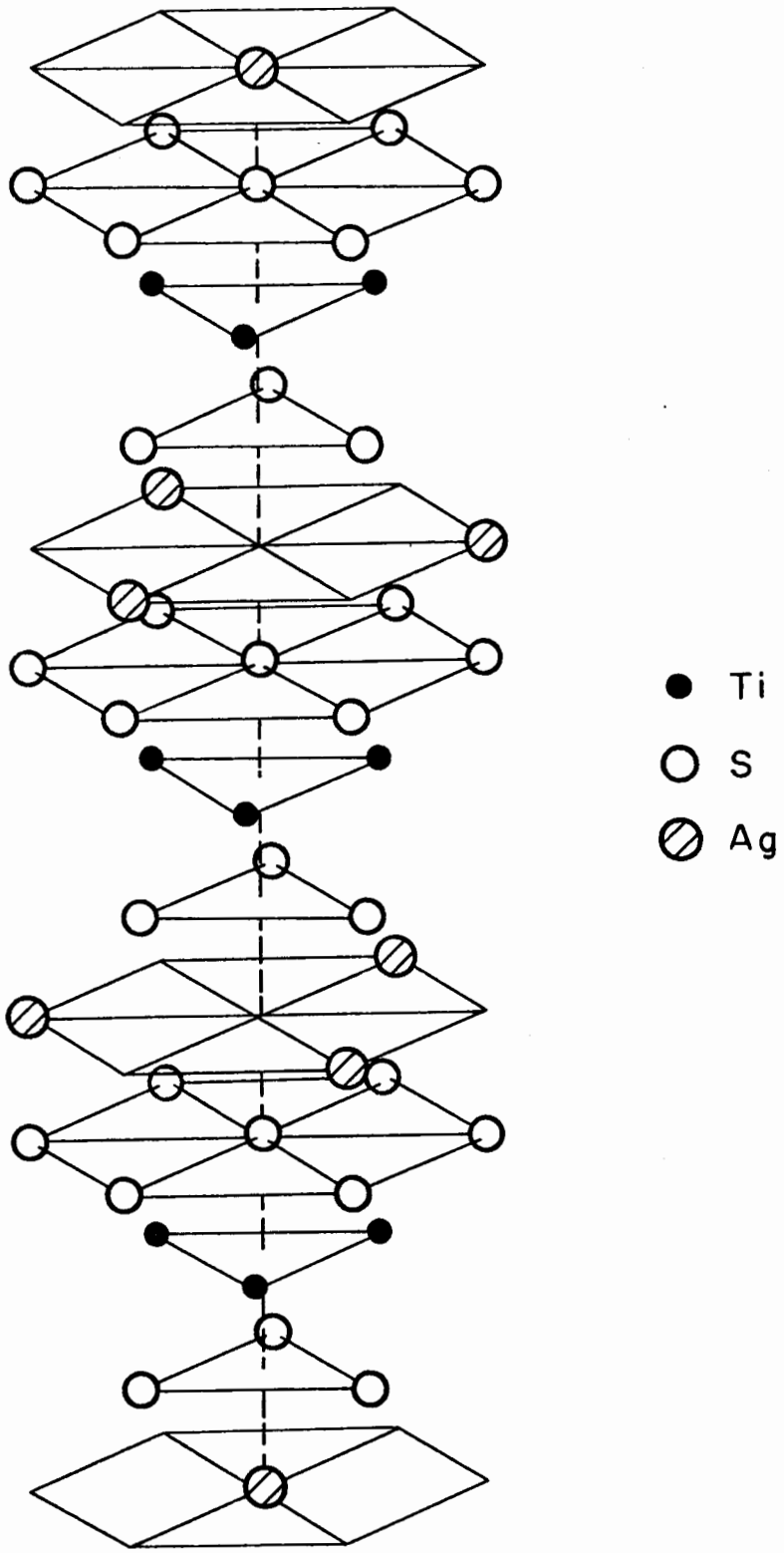

Figure 3.4- Unit cell of $Ag_{1/3}TiS_2$ in the C_3^4 configuration.

for the two above systems are given in Appendix A[2]. The results are summarized in Tables 3.1 and 3.2.

3.7- Symmetry Coordinates

As has been seen in Section 3.1, a knowledge of the dynamical matrix enables a determination of the frequencies of the different normal modes. Such a calculation can be very tedious for a crystal with a primitive cell containing ten atoms but it is usually possible to block diagonalize the dynamical matrix by choosing an appropriate set of coordinates. The eigenvalues and eigenvectors can then be obtained from the different blocks independantly.

Such an appropriate set is comprised by the so-called symmetry coordinates. A symmetry coordinate associated with a representation Γ^{ℓ} satisfies:

$$S_p^{\ell} \xrightarrow{R} (S_p)' = \sum_m D^{\ell}(R)_{mp} S_m^{\ell} \qquad (m,p = 1,\ldots,g^{\ell}) \qquad (41)$$

where g^{ℓ} is the dimensionality of the representation Γ^{ℓ} and $[D^{\ell}(R)]$ is its associated $g^{\ell}xg^{\ell}$ matrix (see Section 3.2).

A method to find the symmetry coordinates is given in Poulet and Mathieu (1970). Let $\{x_i\}$ be a set of 3s coordinates which transform into each other under an operation R according to:

---

[2]For more details on the notation used in finite group theory, see Tinkham (1964).

TABLE 3.1

Irreducible representations of the TiS_2, $Ag_{1/3}TiS_2$ (C_{3i}^2) and $Ag_{1/3}TiS_2$ (C_3^4) crystal point groups.

$\underline{TiS_2}$

Space group D_{3d}^3, point group D_{3d}

1 Ti in (0,0,0), site group D_{3d}

2 S in (1/3,2/3,z), (2/3,1/3,$\bar{z}$), site group C_{3v}

$\Gamma_{Ti} = A_{2u} + E_u$

$\Gamma_S = A_{1g} + A_{2u} + E_g + E_u$

$\Gamma_{crystal} = A_{1g} + 2A_{2u} + E_g + 2E_u$

Raman active: $A_{1g} + E_g$

$\underline{Ag_{1/3}TiS_2}$, $\underline{Ag \text{ in octahedral sites}}$

Space group C_{3i}^2, point group C_{3i}

1 Ag in (0,0,1/2), site group C_{3i}

1 Ti in (0,0,0), site group C_{3i}

2 Ti in (0,0,z_1), (0,0,$\bar{z}_1$), site group C_3

6 S in (x,y,z_2), ($\bar{y}$,x-y,z_2), (y-x,$\bar{x}$,z_2)
($\bar{x}$,$\bar{y}$,$\bar{z}_2$), (y,y-x,$\bar{z}_2$), (x-y,x,$\bar{z}_2$), site group C_1

$\Gamma_{Ag} = \Gamma_{Ti(C_{3i})} = A_u + E_u$

$\Gamma_{Ti(C_3)} = A_g + A_u + E_g + E_u$

TABLE 3.1 (continued)

$\Gamma_S = 3A_g + 3A_u + 3E_g + 3E_u$

$\Gamma_{crystal} = 4A_g + 6E_u + 4E_g + 6E_u$

Raman active: $4A_g + 4E_g$

$\underline{Ag_{1/3}TiS_2}$, Ag in tetrahedral sites

Space group C_3^4, point group C_3

1 Ag in $(0,0,z_1)$, site group C_3

1 S in $(0,0,0)$, site group C_3

1 S in $(0,0,z_2)$, site group C_3

1 S in $(0,0,\bar{z}_2)$, site group C_3

3 S in (x_3,y_3,z_3), $(\bar{y}_3,x_3-y_3,z_3)$, $(y_3-x_3,\bar{x}_3,z_3)$, site group C_1

3 Ti in (x_4,y_4,z_4), $(\bar{y}_4,x_4-y_4,z_4)$, $(y_4-x_4,\bar{x}_4,z_4)$ site group C_1

$\Gamma_{Ag} = \Gamma_{S(C_3)} = A + E$

$\Gamma_{S(C_1)} = \Gamma_{Ti} = 3A + 3E$

$\Gamma_{crystal} = 10A + 10E$

Raman active: 10A +10E

TABLE 3.2

Raman tensors of the active modes for the D_{3d}, C_{3i} and C_3 point groups.

	$\begin{pmatrix} a & & \\ & a & \\ & & b \end{pmatrix}$	$\begin{pmatrix} c & & \\ & -c & d \\ & d & \end{pmatrix}$	$\begin{pmatrix} & -c & d \\ -c & & \\ -d & & \end{pmatrix}$
D_{3d}:	A_{1g}	E_g	E_g
	$\begin{pmatrix} a & & \\ & a & \\ & & b \end{pmatrix}$	$\begin{pmatrix} c & d & e \\ d & -c & f \\ e & f & \end{pmatrix}$	$\begin{pmatrix} d & -c & -f \\ -c & -d & e \\ -f & e & \end{pmatrix}$
C_{3i}:	A_g	E_g	E_g
C_3:	A(z)	E(x)	E(y)

$$x_i \xrightarrow{R} x_i' = \sum_j R_{ij} x_j \tag{42}$$

Then one can obtain a symmetry coordinate S_p^{ℓ} from the x_i's by forming the following expression:

$$S_p^{\ell} = C \sum_R [D^{\ell}(R)^*_{mp} \sum_j R_{ij} x_j] \tag{43}$$

where C is a normalization factor. In view of the experimental results described in the next chapter, it was considered sufficient to evaluate only the part of the dynamical matrix corresponding to the Raman active phonons of A-type symmetry.

For the four A_g representations of the C_{3i}^2 configuration and the ten A representations of the C_3^4 configuration, one can see from the character tables given in appendix A that $[D^{\ell}(R)] = [1]$. Therefore, for those species, equation (43) simplifies to:

$$S^{\ell} = \sum_R R_{ij} x_j \tag{44}$$

where the subscript p has been dropped since $g^{\ell} = 1$.

The transformation relations (42) are given in appendix B. The symmetry coordinates corresponding to the A-type Raman active phonons of both configurations are given in Table 3.3 and Figure 3.5.

TABLE 3.3

Symmetry coordinates corresponding to the A-type Raman active phonons of the C_{3i}^2 and C_3^4 configurations.

C_{3i}^2

$$S^1 = -x_5 + \tfrac{1}{2}(-x_6 - \sqrt{3}y_6) + \tfrac{1}{2}(x_7 + \sqrt{3}y_7)$$
$$+x_8 + \tfrac{1}{2}(-x_9 - \sqrt{3}y_9) + \tfrac{1}{2}(-x_{10} - \sqrt{3}y_{10})$$
$$S^2 = y_5 + \tfrac{1}{2}(-\sqrt{3}x_6 - y_6) + \tfrac{1}{2}(\sqrt{3}x_7 - y_7)$$
$$-y_8 + \tfrac{1}{2}(\sqrt{3}x_9 + y_9) + \tfrac{1}{2}(-\sqrt{3}x_{10} + y_{10})$$
$$S^3 = z_3 - z_4$$
$$S^4 = (z_5 + z_6 + z_7) - (z_8 + z_9 + z_{10})$$

C_3^2

$$S^1 = x_5 + \tfrac{1}{2}(-x_6 + 3y_6) + \tfrac{1}{2}(-x_7 - 3y_7)$$
$$S^2 = -y_5 + \tfrac{1}{2}(3x_6 + y_6) + \tfrac{1}{2}(-x_7 + y_7)$$
$$S^3 = z_5 + z_6 + z_7$$
$$S^4 = -x_8 + \tfrac{1}{2}(x_9 - \sqrt{3}y_9) + \tfrac{1}{2}(x_{10} + \sqrt{3}y_{10})$$
$$S^5 = y_8 + \tfrac{1}{2}(-\sqrt{3}x_9 - y_9) + \tfrac{1}{2}(\sqrt{3}x_{10} - y_{10})$$
$$S^6 = z_8 + z_9 + z_{10}$$
$$S^7 = z_2$$
$$S^8 = z_3$$
$$S^9 = z_4$$
$$S^{10} = z_1$$

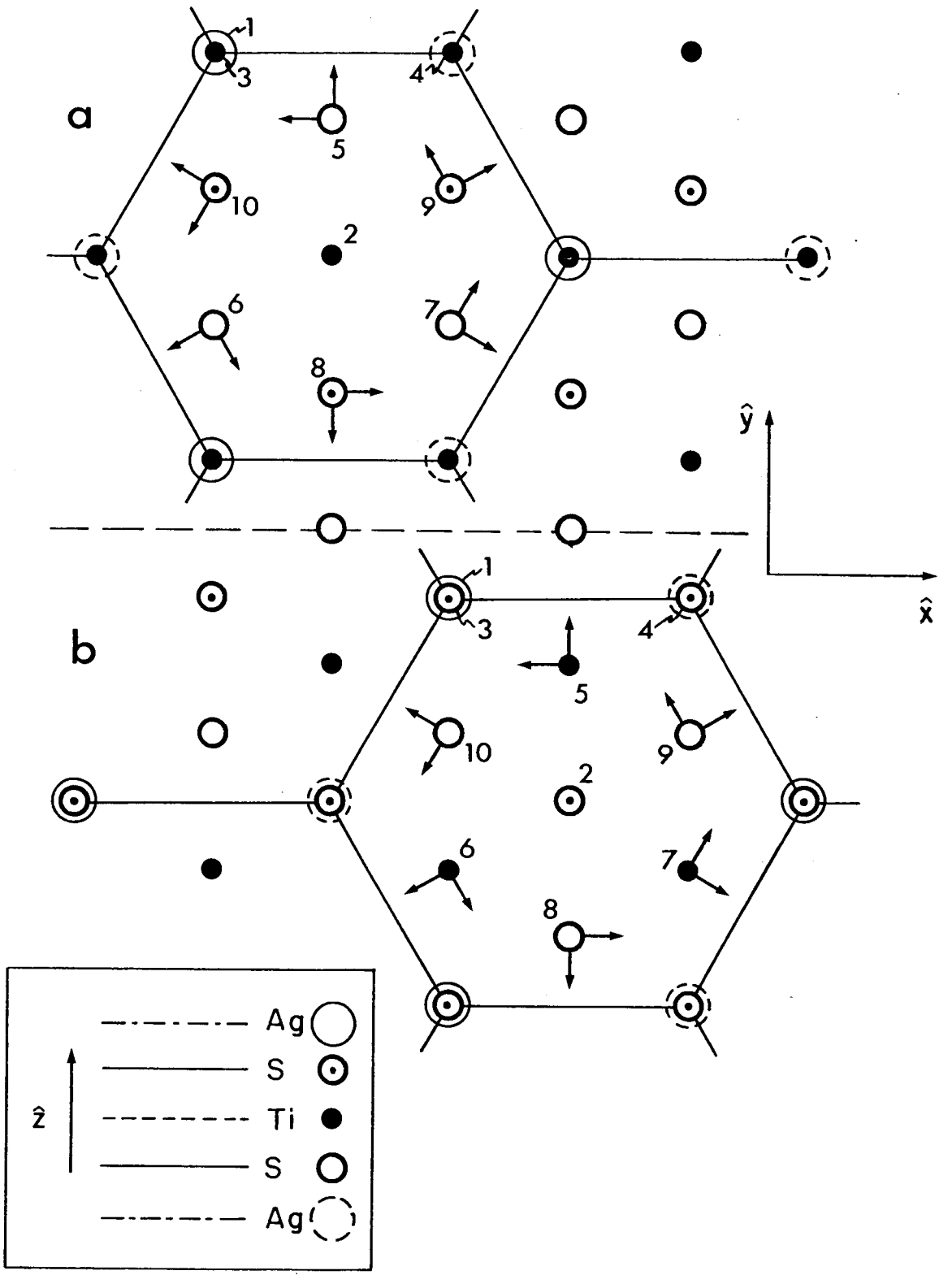

Figure 3.5- In-plane components of the symmetry coordinates. a) C^2_{3i} configuration. b) C^4_3 configuration. Inset: schematic representation of the succession of layers.

3.8- Effect of Disorder on the Scattering Intensity

The effect of disorder on the physical properties of a crystal is difficult to predict. Although some quantitative calculations can be performed in the limiting cases of complete and small disorder, in most of the cases one is left with only qualitative predictions[3]. Thus, the discussion found below is intended to set limits on the effects of an order-disorder phase transition on the scattering intensity.

If the order of the silver superlattice is significantly altered, it is not possible to use (27) in the expression (24). Instead of (33), one is thus left with:

$$I_2 = C \sum_{\alpha\beta\alpha'\beta'} \sum_{mj\gamma} \sum_{m'j'\gamma'} P_{\alpha\beta,\gamma}(mj) P^*_{\alpha'\beta',\gamma'}(m'j') e_{1\beta} e_{1\beta'} e_{2\alpha} e_{2\alpha'} \times \int_{-\infty}^{\infty} e^{i\omega t} (\omega_1+\omega)^4 \langle u_\gamma(mj,t) u_{\gamma'}(m'j',0)\rangle dt \qquad (45)$$

Equation (45) contains in it the possibility that some scattering is caused by localized modes. But any extra feature in the Raman spectra induced by zone-folding requires that atoms vibrate in phase on a scale large compared to the unit cell dimensions. Hence, if the long range ordering of the silver atoms is altered, such a feature should decrease in intensity because, first, a certain fraction of the silver atoms are displaced so that the unit cell in which they sat does not contribute in phase to the scattering process anymore and

---

[3]Maradudin et al. (1971) have devoted a full chapter to the effect of disorder on the lattice vibrations.

second, because a displaced atom will perturb its neighbours and thus modify the contribution to the scattering intensity of their cell.

If one assumes that it is possible to separate the spatial average from the ensemble and time averages in (45), then one can attempt to isolate the effect of the disordering of the silver atoms by writing:

$$I' = X(T) \sum_{ij} C_{ij} \qquad (46)$$

where I' is the intensity of an extra mode arising from the presence of silver atoms and where $C_{ij} = 1$ if ions i and j are on the same sublattice (A, B or C) and -1/2 if not. With such a definition, I'/X(T) is maximum when the sites of only one sublattice are occupied and vanishes when the occupation fractions x_A, x_B and x_C are equal.

Now, let $\varphi(L,L')$ be the probability that any pair of atoms i and j be respectively on site L and L' (L, L'= A, B or C). Then, one has:

$$\sum_{ij} C_{ij} \propto \varphi(A,A) + \varphi(B,B) + \varphi(C,C) - \varphi(A,B) - \varphi(A,C) - \varphi(B,C) \qquad (47)$$

In the mean field approximation,

$$\varphi(L,L') = x_L x_{L'} \qquad (48)$$

so that:

$$\sum_{ij} C_{ij} \propto x_A^2 + x_B^2 - 2x_A x_B \qquad (49)$$

since x_B is equal to x_C.

On the other hand, the order parameter η, given by equation 2.10, can be written as:

$$\eta = x_A - x_B \qquad (50)$$

Compairing (49) and (50) yields:

$$\sum_{ij} C_{ij} \propto \eta^2 \qquad (51)$$

Thus, it is reasonable to expect that the intensity of any extra feature in the Raman spectrum induced by a zone-folding mechanism should vanish somewhat like η^s with $s \sim 2$.

IV. Experimental Procedures and Results

4.1- Sample Preparation

The TiS_2 crystals were supplied by Dr. R. F. Frindt in the form of thin platelets several millimeters across. They were grown by iodine vapor transport at 600°C from a stoichiometric mixture of the constituent elements.

Stoichiometric TiS_2 is difficult to obtain but standard growth procedures reliably give crystals with deviation from stoichiometry of less than 5% (Benard and Jeannin, 1965, Thompson et al, 1975).

Several platelets were repeatedly cleaved using "invisible Sellotape" brand adhesive tape. The cleaved portions were then detached from the adhesive tape by dissolving the glue in trichloroethylene.

Samples for intercalation were cut from the good looking portions of the recuperated crystals in rectangular shapes of approximately 1 mm x 0,5 mm and weighed to within 0,5 µg with a Cahn model G-2 electrobalance. Their thicknesses were evaluated from their mass to surface area ratio. The samples retained had masses ranging between 10 and 30 µg and thicknesses of 4 to

6 μm.

The crystals were then mounted in a cell adapted from a design by Dr. J. Chiu, from the Department of Physics of the University of British Columbia (see Fig. 4.1). The electrolyte was an aqueous solution of 1M-$AgNO_3$. The contacts were produced by evaporating nickel on a microslide and annealing it under vacuum at 300 C for about one hour. The TiS_2 and Ag electrodes were partially covered with parts of the neoprene gasket to maintain them in position and ensure a good electrical contact. The cell was sealed with silicon vacuum grease and maintained assembled with small hose cut-off clamps. The intercalation was allowed to proceed by connecting the TiS_2 cathode with the Ag anode through an external resistor and could be followed under a microscope.

In order to assess the silver content of the crystals, coulometric titration was tried but found unreliable because of important contributions from side reactions. The composition was therefore determined by weighing the crystals after intercalation.

During the intercalation process, a first front was seen to develop from the edges of the crystals and from defects on the surfaces. The crystals would go from golden-coloured to greyish and they would start to buckle. Then a second front would develop behind the first one, identified by a darker grey colour on reflection and accompanied by fractures perpendicular to the

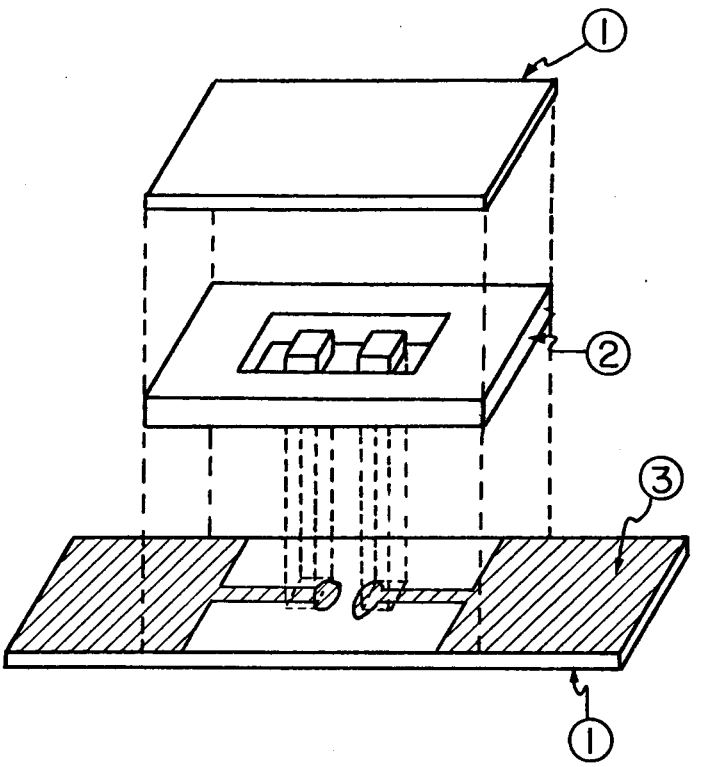

① Glass microslide

② Neoprene gasket

③ Evaporated nickel contact

Figure 4.1- Intercalation cell.

edges of the crystals.

After several hours of discharge, the fronts would extend over the entire surface and the crystals would acquire a uniform colour.

Crystals with composition in the range $0 < x < 0,66$ were obtained by stopping the discharge after periods ranging from one hour to several days. The crystals were then removed from the bath and left at room temperature for periods of up to several weeks in order to ensure uniformity.

The characteristics of the four crystals on which most of the Raman work described in Section 4.5 was done are given in Table 4.1.

The crystals retained for further analysis were glued on small copper disks with Eccobond PDQ fast curing epoxy adhesive. The copper disks were mounted on the cold finger of an Air Products Displex closed-cycle refrigeration system model CSW-202. The temperature of the cold finger could be varied between 10 K and 300 K.

4.2- The Raman Spectroscopy Apparatus

The Raman spectra were obtained from the freshly cleaved faces of the Ag_xTiS_2 crystals. They were excited with the 514,5 ηm line of a Spectra Physics model 165 ion argon laser. It was decided to perform the experiments in the backscattering

TABLE 4.1

Ag_xTiS_2 samples.

Dimensions	Mass before intercalation (µg)	Mass after intercalation (µg)	Composition x
2,8 mm x 0,5 mm x 6 µm	28,6±0,5	33,9±0,5	0,19±0,01
1,6 mm x 0,4 mm x 4 µm	8,8±0,5	11,5±0,5	0,33±0,03
∿ 3 mm x ∿ 3 mm x ?	1230	1720	0,41*
1,8 mm x 0,5 mm x 5 µm	14,3±0,5	23,2±0,5	0,65±0,05

* Sample supplied by P. Joensen.

geometry (see Fig. 4.2). Such a geometry prevented excessive heating of the samples and gave a better signal to noise ratio than the 90^0 geometry, given the relatively poor surface quality of the crystals, even after cleavage.

The laser beam was sent through an interference filter to eliminate spurious laser lines and was weakly focussed by a cylindrical lens with a 10 cm focal length. This produced a line of about 2 mm X 20 μm on the crystals. Approximately 30% of the beam intensity emitted by the laser reached the sample, due to secondary reflections in several prisms and also because of the absorption from the filter. The laser power output was kept at 800 mw for most of the spectra, thus giving a power density of about 6 watt/mm^2 on the crystal.

The scattered light was collected by a lens and sent through a quartz wedge, to eliminate polarization effects on the gratings. The light was then focussed on the entrance slit of a Spex model 14018 Czerny-Turner 0,85 m double monochromator equipped with holographic gratings having 1800 grooves/mm. The double monochromator was followed by a single grating monochromator (Spex model 1442) to further reduce the intensity of the stray light.

The signal was detected with a RCA model C31034-A photomultiplier housed in a Products for Research model TE-104 refrigeration chamber. The output pulses were fed into an Ortec model 9301 fast amplifier followed with an Ortec model 9302

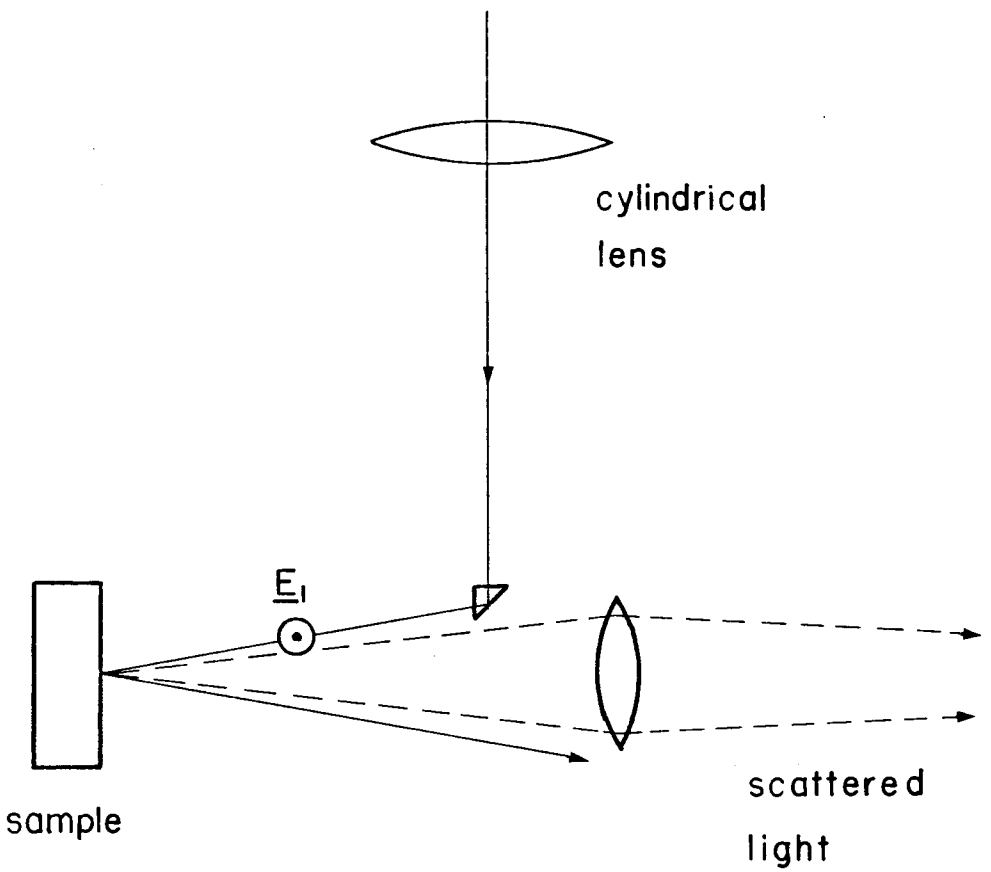

Figure 4.2- The backscattering geometry.

amplifier-discriminator. The discriminator voltage was adjusted to maintain a dark count of about 10 cps. The discriminator output could be fed into a pulse counter or into an Ortec model 9349 ratemeter connected to a strip chart recorder.

The system could be controlled manually or with a PDP 11/10 minicomputer which could step the spectrometer and read the pulse counter mentioned above. The software in the computer allowed it to scan in succession up to five different regions of the spectrum. It was found that performing several shorter scans rather than a long one was preferable because it eliminated variations in the spectra caused by small changes in the optical alignment over long periods of time, thus enabling a more accurate measurement of the relative intensities of different peaks. The computer was also used to remove background from the data.

The slits of the spectrometer were opened to 350 μm. This gave a resolution better than 4 cm^{-1}, as measured from the half-width of the spurious laser lines. The data points were taken at intervals of 1 cm^{-1} and were smoothed using a five point convoluting procedure which generated smoothed points from the original data points according to:

$$Y'_j = \frac{1}{N} \sum_{i=-2}^{2} C_i Y_{j+i} \qquad (1)$$

where Y'_j and Y_j represent the intensity data points for the smoothed and unsmoothed data respectively. The convoluting

integers C_i are -3,12,17,12,-3, as given by Savitzky and Goley (1964).

4.3- Symmetry Assignation

The polarization analysis of the Raman peaks was done by inserting a Glan-Thompson prism between the collecting lens and the quartz wedge.

The impinging beam had its polarization components along the a and b crystal axes only. With such a geometry, the light scattered from an A-type vibrational mode has the same polarization as the incident light while the light scattered from an E-type mode has mixed polarization components, as can be seen from the Raman tensors shown in Table 3.2.

This means that when the axis of the Glan-Thompson prism and the polarization of the incident light are parallel, both A and E-type modes appear, while when they are perpendicular, only the E-type modes are observed.

4.4- Temperature Determination

Whenever a Raman Stokes peak was intense enough, a spectrum was taken in the corresponding anti-Stokes region. The actual temperature of the illuminated portion of the crystals could then be determined using equation 3.40. The scattered intensity

was assumed proportional to the area under the peaks whose width was much greater than the instrumental resolution.

At 515 ηm, the absorption coefficient of TiS_2 is about $5x10^{-7}m^{-1}$ (see Figure 2.2). This gives a penetration length of around 20 ηm. This dimension is much smaller than the thickness of the samples which in turn is much smaller than the linear dimensions of the illuminated area. One can thus approximate the steady state by a linear heat flow in a slab with a surface held at the ambient temperature T_1 and the opposite one heated by the incident radiation. The relevant equation is:

$$T - T_1 = \frac{\dot{Q}w}{\kappa A} \qquad (2)$$

were $\dot{Q}$ is the thermal energy flow, w the thickness of the crystal, A its surface area and κ the thermal conductivity.

With the power output at 800 mw, it turned out that the temperature measured by the anti-Stokes to Stokes ratio was between 20 K and 60 K above the temperature of the cold finger. Such a spread can be explained by variations in the area A due to differences in the incident angle and the focussing of the laser beam. Also to be considered are variations in the flow $\dot{Q}$ due to differences in the smoothness of the surfaces and variations of the thermal conductivity with temperature, composition and possibly with an order-disorder phase transition. None of those factors could easily be controlled so that when the temperature could not be determined with enough

accuracy by the anti-Stokes to Stokes ratio, it was assumed to be 40 K ±20 K above the temperature of the cold finger.

4.5- Experimental results

Raman spectra of pure TiS_2 are shown in Figure 4.3. The symmetry assignment has previously been done by Smith et al. (1972).

The frequency of the peaks shift to lower values as the temperature is increased, as can be seen from Figure 4.4. Also, there is a second order "shoulder" on the A_{1g} peak that grows with temperature.

Figures 4.5 and 4.6 show Raman spectra of the $Ag_{0,19}TiS_2$ sample at different temperatures. One can see that three new features, labeled A_1, A_2 and A_3, are induced. The sample was cleaved on several occasions between scans and the laser beam was moved across it. Although some variation in intensity was observed, the peaks were always visible and their frequencies did not vary. This indicates a good uniformity. The new peaks were seen to disappear at about 280 K.

It is to be noted that only the spectrum at T= 90 K was taken using the third monochromator. The low frequency tail seen in the T= 230 K is thus mostly due to stray light.

Figure 4.7 shows the spectra taken from the $Ag_{0,33}TiS_2$ sample. The A_{1g} peak intensity is dramatically reduced with

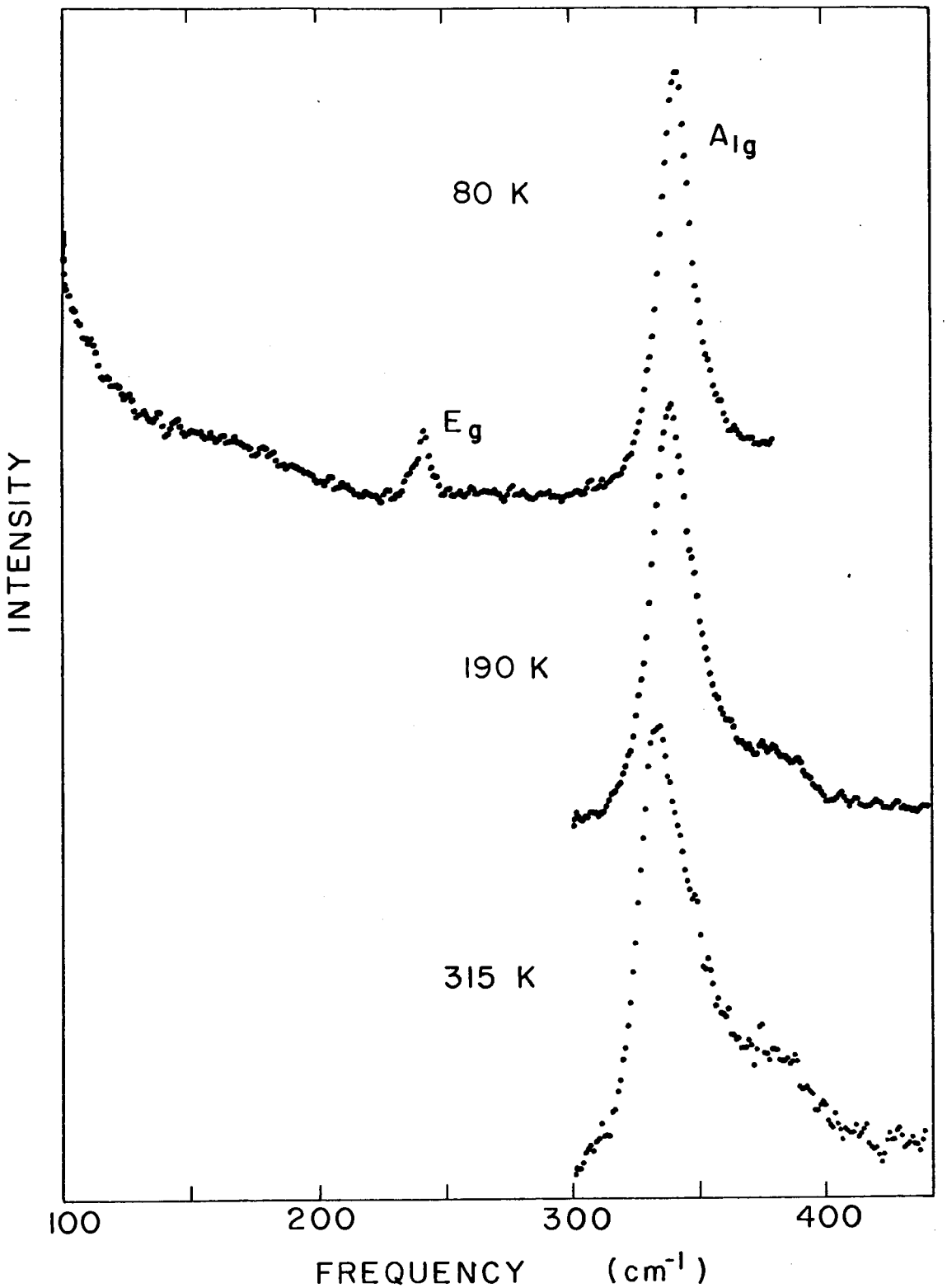

Figure 4.3- Raman spectra of TiS_2.

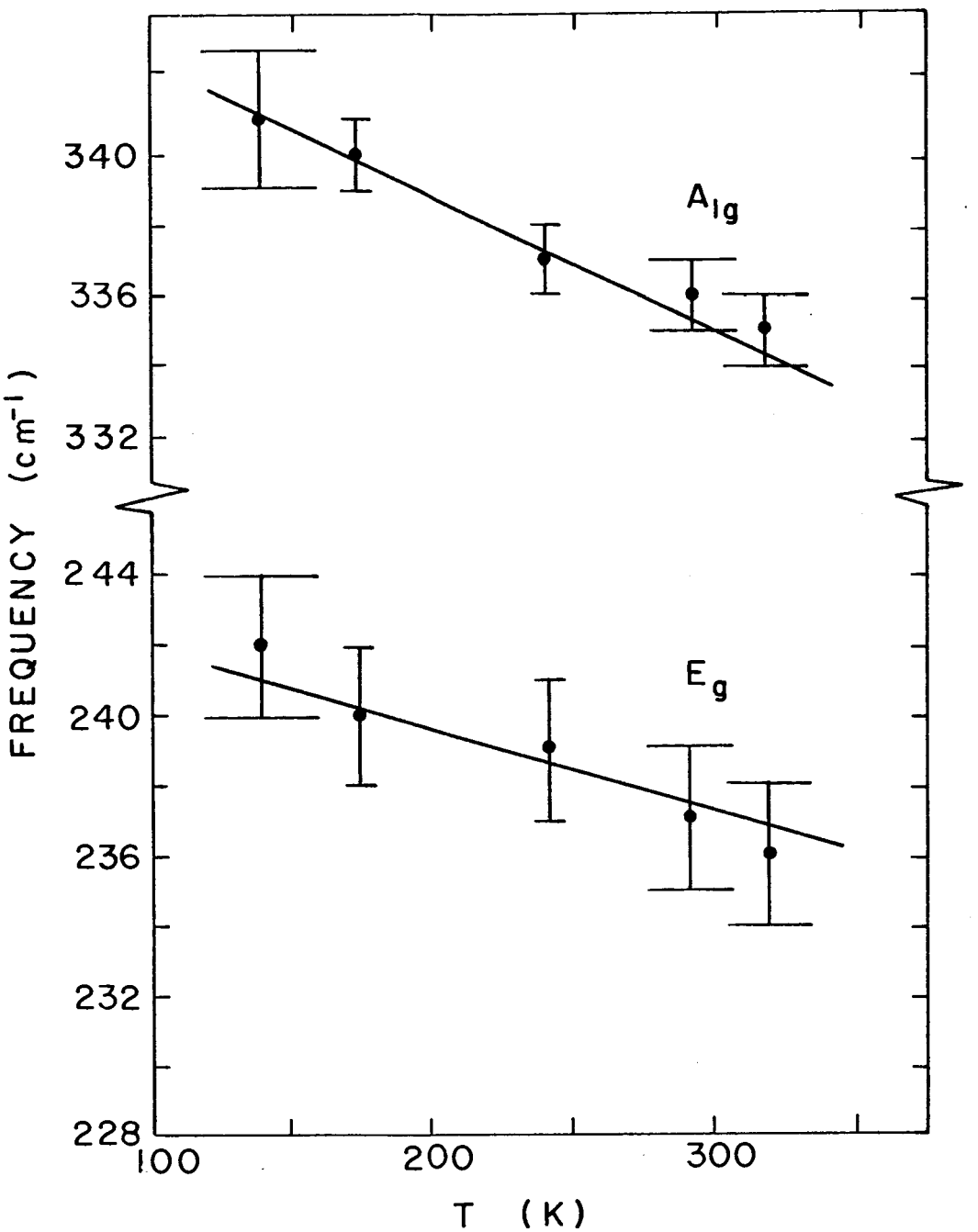

Figure 4.4- Frequency of the A_{1g} and E_g modes in pure TiS_2 as a function of temperature. The solid lines give the linear least sqare fits of the data points.

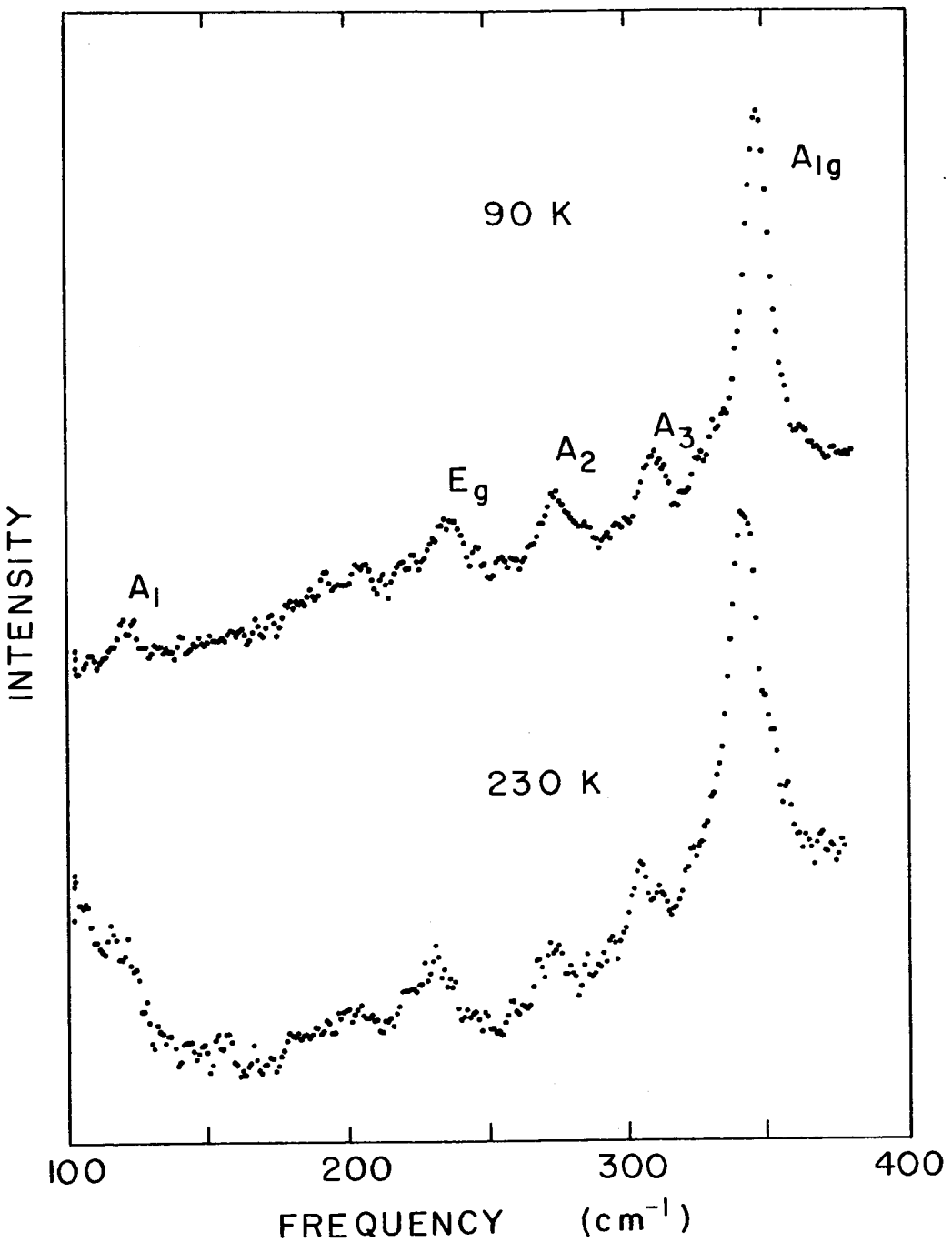

Figure 4.5- Raman spectra of $Ag_{0,19}TiS_2$ with T <250 K.

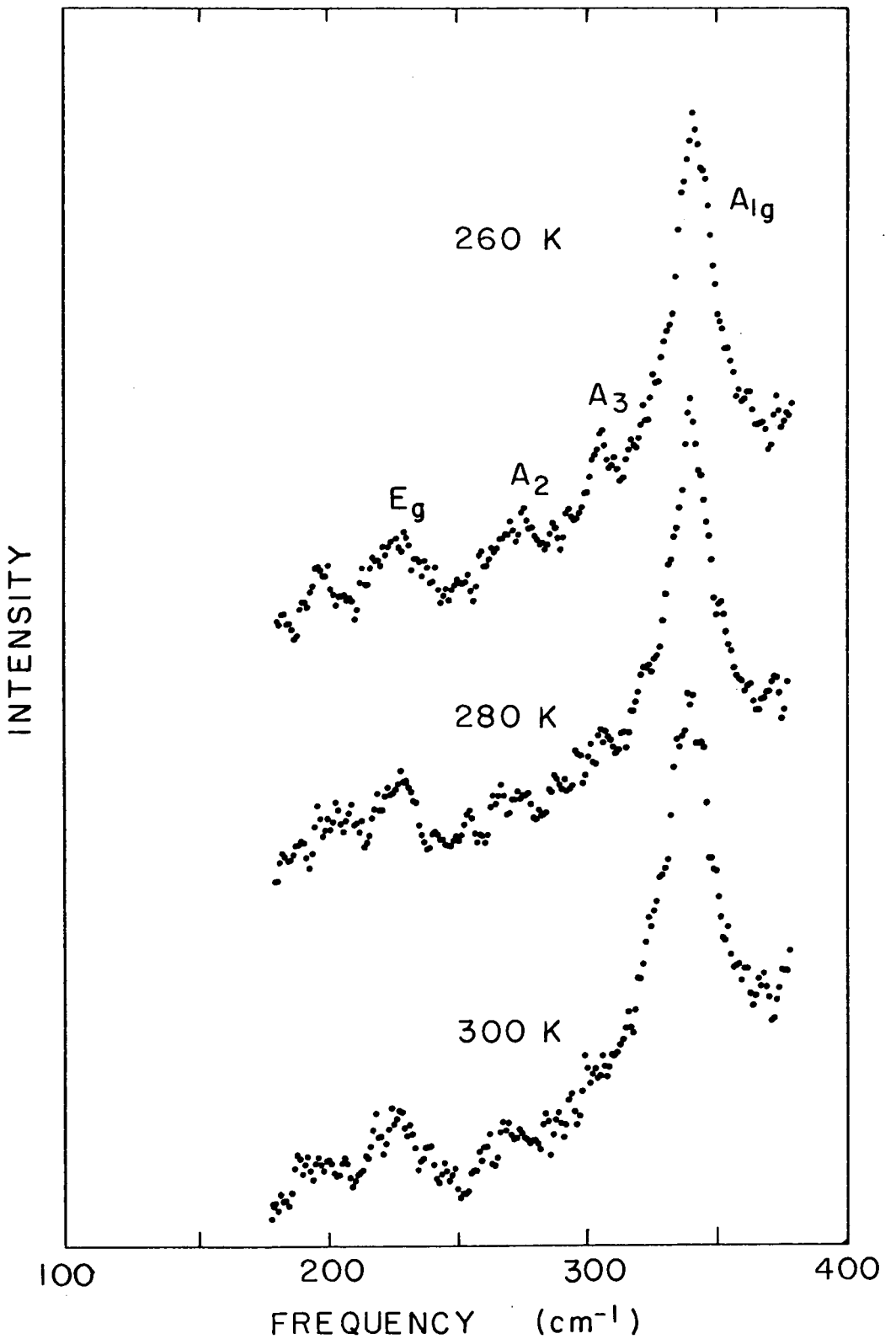

Figure 4.6- Raman spectra of $Ag_{0,19}TiS_2$ with T > 250K.

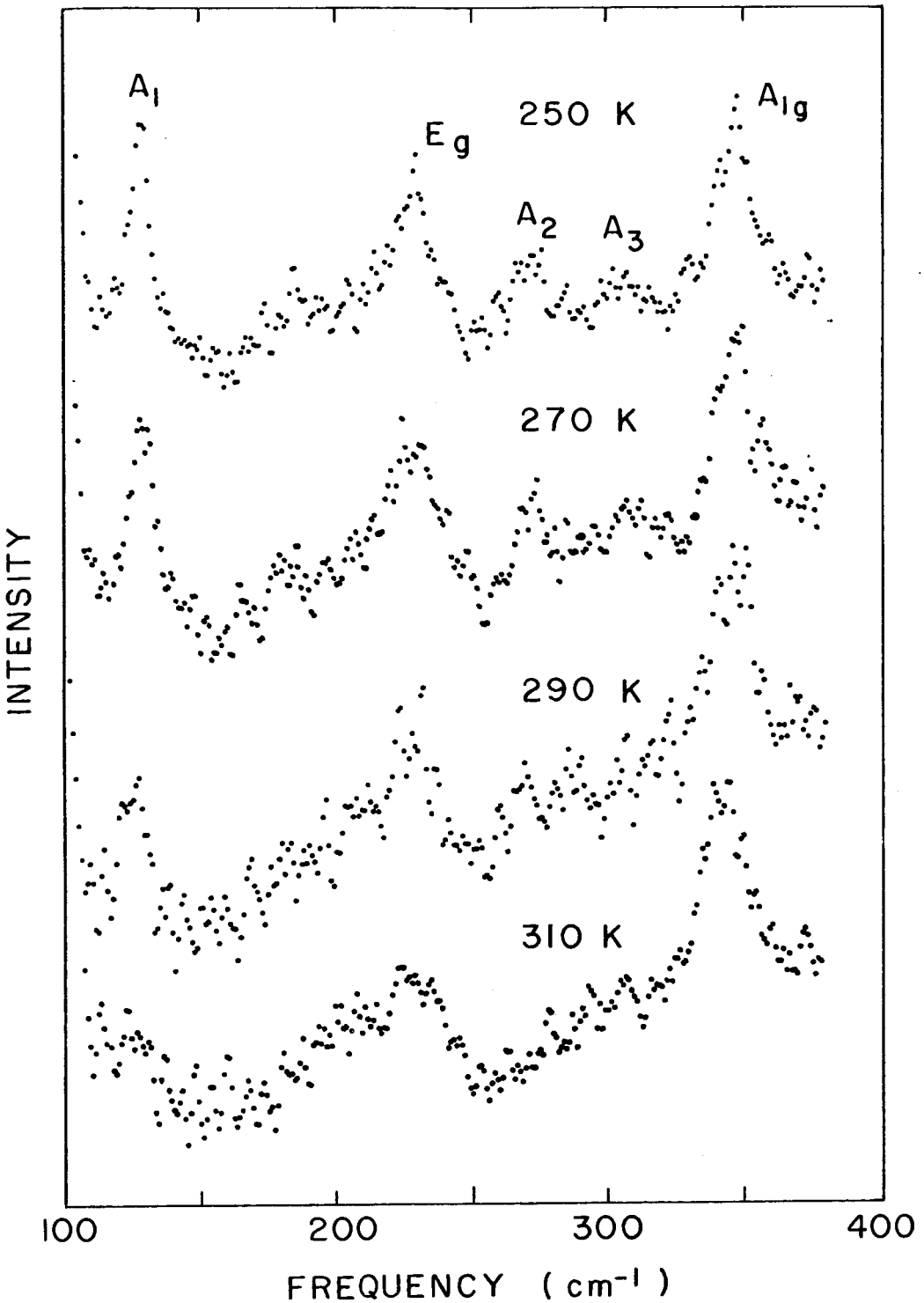

Figure 4.7- Raman spectra of $Ag_{0,33}TiS_2$.

respect to the E_g peak intensity. The A_2 and A_3 peaks are still discernable and the A_1 peak is now a prominent feature. It can be seen to disappear in the vicinity of 300 K. All the spectra on Figure 4.7 were taken using the third monochromator.

Figure 4.8 shows spectra obtained from the $Ag_{0,41}TiS_2$ and $Ag_{0,65}TiS_2$ samples. They were taken manually with an integration constant of 10 s. The spectra are very similar and exhibit A_{1g} and E_g peaks with near equal intensities together with a sharper A_1 peak. The A_2 and A_3 peaks could not be seen.

Figure 4.9 shows two series of spectra taken from samples different from the ones described above. The composition x was 0,25 for the spectra (a) and (b) and 0,33 for the spectra (c) and (d). Spectra (a) and (c) show the diagonal components of the peaks while spectra (b) and (d) show only the non-diagonal components. Those spectra clearly reveal that all the new peaks have an A-type symmetry (hence the notation A_1, A_2 and A_3).

Figure 4.10 gives the peak frequencies observed for the $Ag_{0,19}TiS_2$ and the $Ag_{0,33}TiS_2$ samples as a function of temperature and Table 4.2 gives their half-width.

Figure 4.11 gives the variation of intensity of the A_1, A_2 and A_3 peaks as a function of temperature. The data points represent the relative intensity of a given peak with respect to the intensity of the A_{1g} peak of the same spectrum. They were further normalized in such a way that the highest ratio for each set of data points was assigned a value of 1.

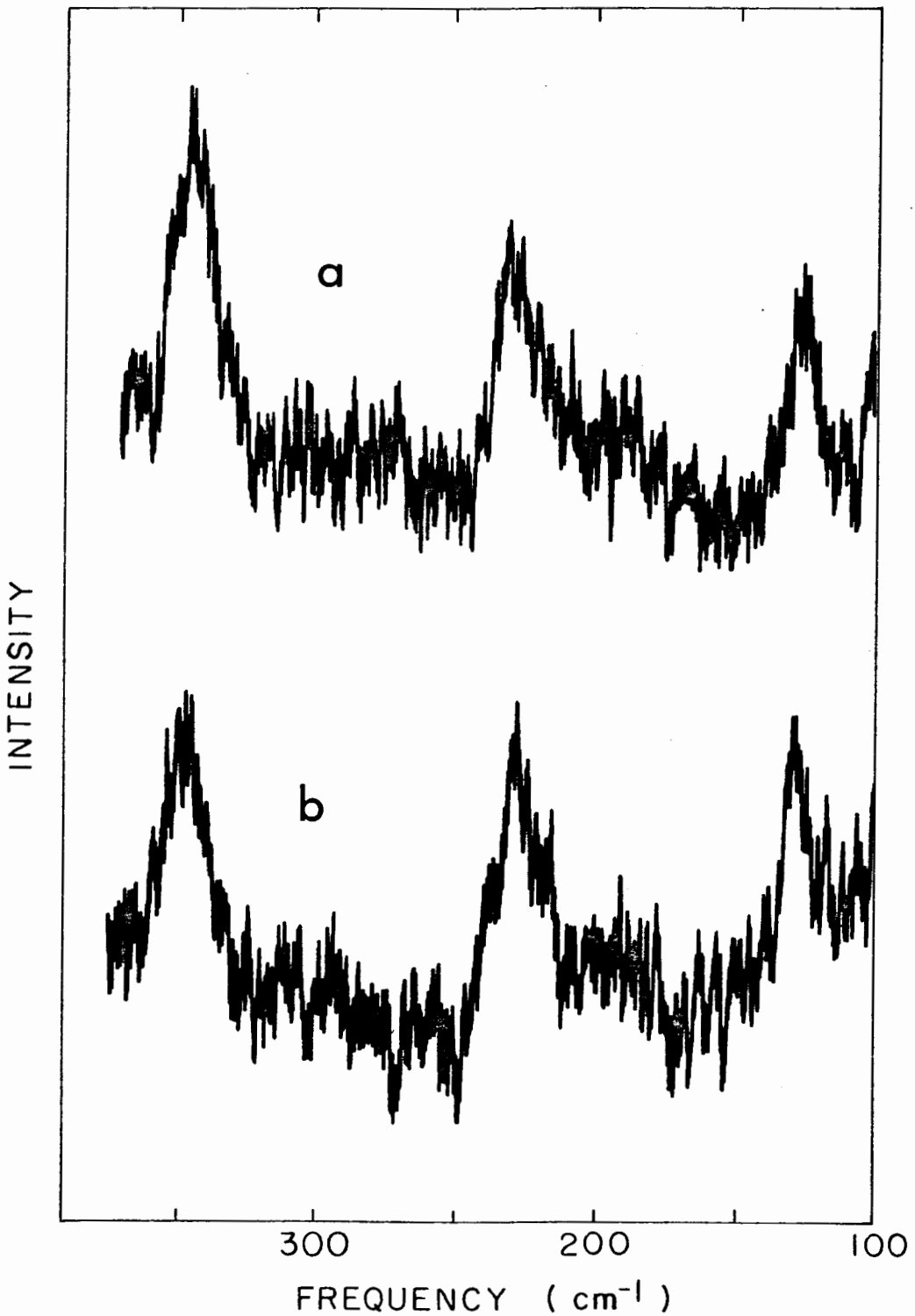

Figure 4.8- Raman spectra of $Ag_{0,41}TiS_2$ (a) and $Ag_{0,65}TiS_2$ (b). Both spectra were taken at T ~ 200 K.

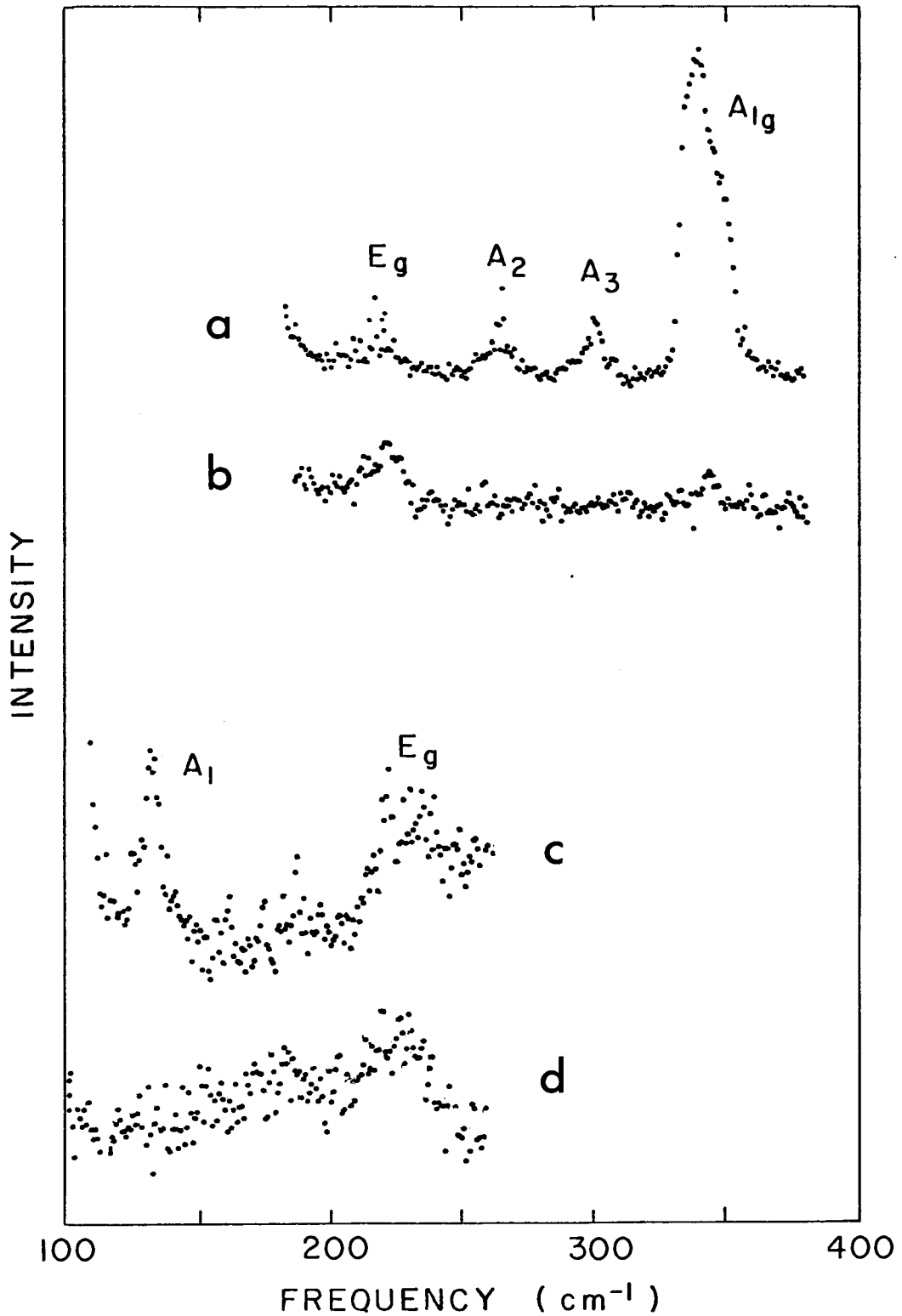

Figure 4.9- Polarization components of the Raman peaks. a) and b) x≃ 0,25; c) and d) x≃ 0,33; a) and c) diagonal components; b) and d) non-diagonal components.

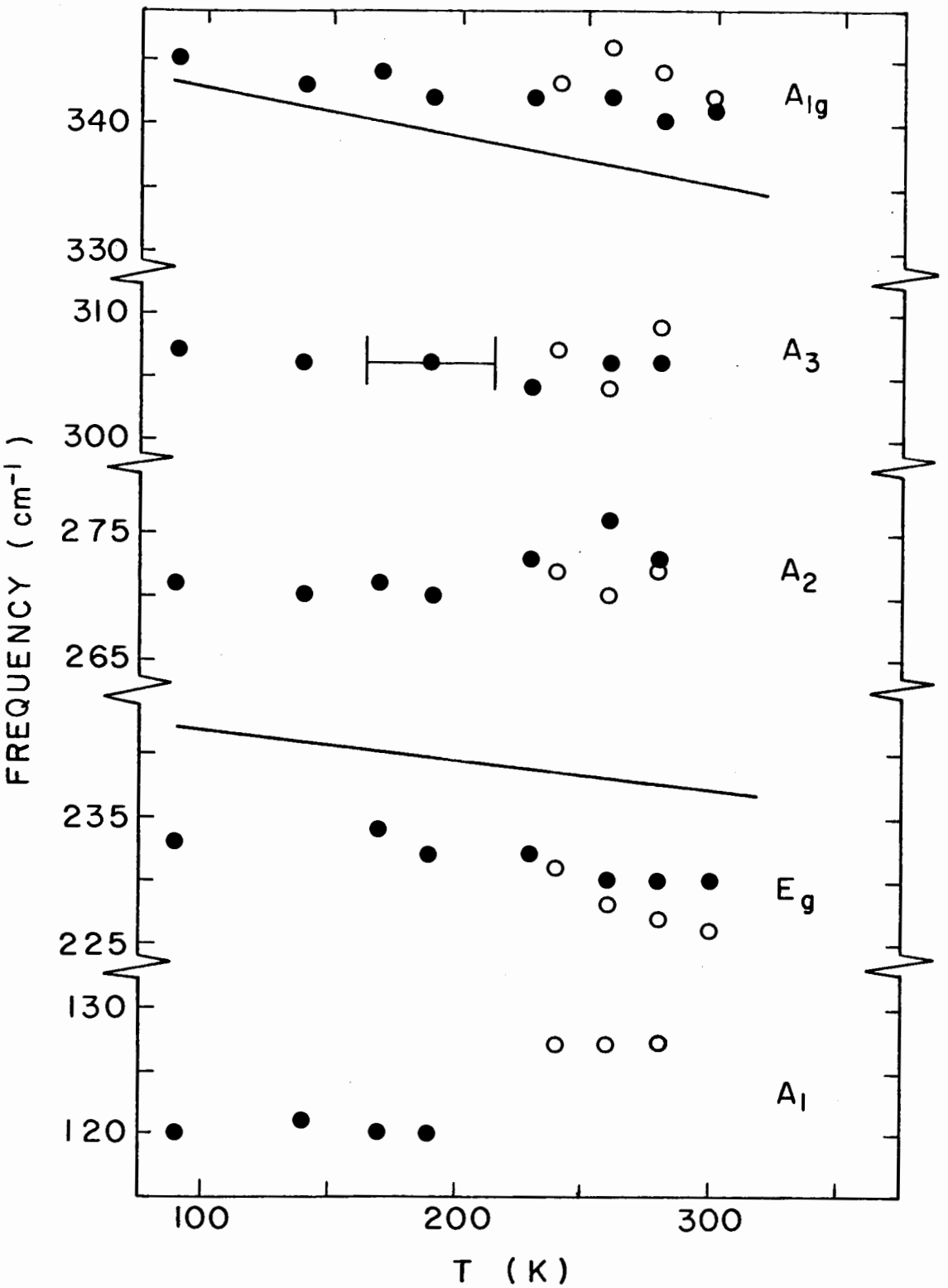

Figure 4.10- Frequency of the Raman peaks in Ag_xTiS_2 as a function of temperature. ● x= 0,19; ○ x= 0,33. The solid lines are the linear fits for the A_{1g} and E_g frequencies as shown in Figure 4.6.

TABLE 4.2

Half-widths of the A_{1g}, E_g, A_1, A_2 and A_3 peaks as a function of composition.

x in Ag_xTiS_2	Half-width (in cm^{-1})				
	A_{1g}	E_g	A_1	A_2	A_3
0,0	10±1	8±1			
0,19	7,5±1	8±1		6,5±2	6,5±2
0,33	11±2	12±2	5±1		

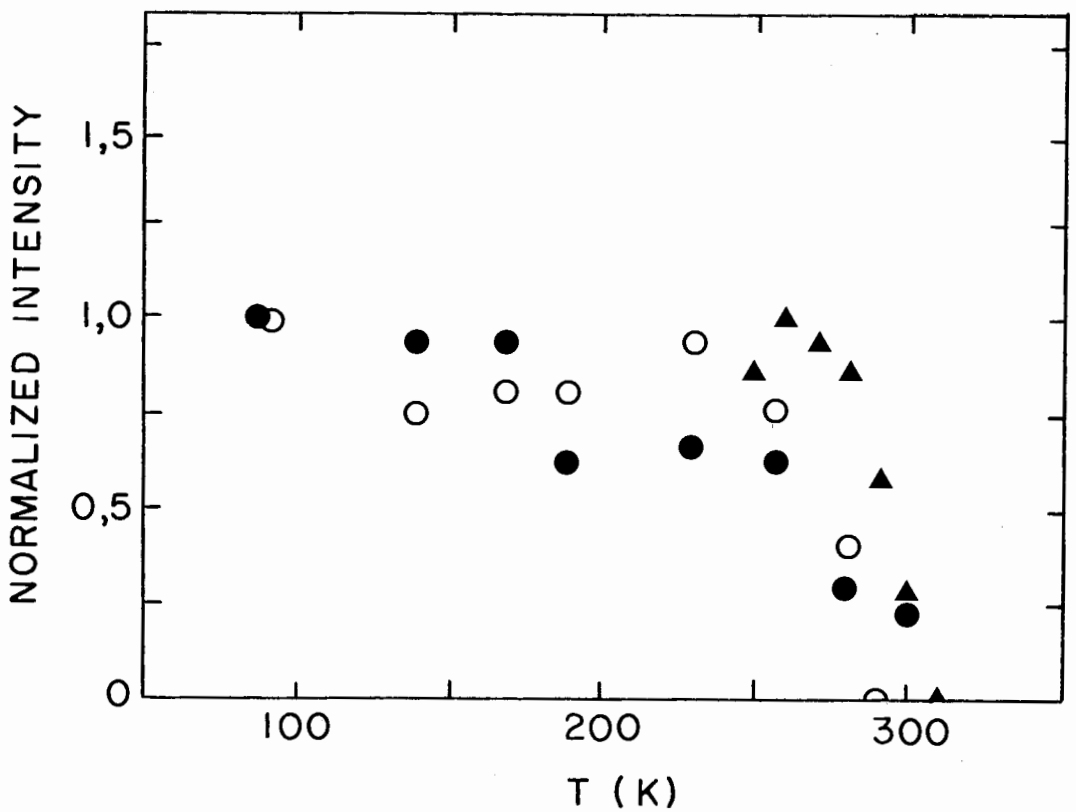

Figure 4.11- Normalized intensity of the A_1, A_2 and A_3 Raman peaks as a function of temperature. ▲ A_1 peak; ● A_2 peak; O A_3 peak.

The points on the abscissa indicate that the corresponding peaks could no longer be seen over the noise.

V. Discussion of the Results

The fact that the frequencies of the A_{1g} and E_g phonons are nearly unaffected by the intercalation of silver in TiS_2 indicates that the interaction of the silver ions with the host layers is small compared to the intralayer interactions.

It therefore seems improbable that the frequency of an oscillatory motion of the silver ions would be comparable with the frequencies of the lattice phonons. The A_1, A_2 and A_3 peaks are thus more likely to come from titanium or sulphur vibrations due to a zone-folding mechanism.

In order to verify this assumption, two simple models were developed. One describes the dynamics of the host structure in order to evaluate the frequencies of the folded back phonons. The other describes the silver-silver interaction and provides a semi-quantitative prediction of the behaviour of the system at the order-disorder phase transition. They are presented in the sections below.

5.1- The Valence Force Field Model

The $\underline{k}= \underline{0}$ frequencies of the Raman active phonons can be obtained from the $\underline{k}= \underline{0}$ expression of the dynamical matrix:

$$F_{\alpha\beta}(jj',\underline{0}) = (M_j M_{j'})^{-\frac{1}{2}} \sum_{m'} \phi_{\alpha\beta}(mj,m'j') \qquad (1)$$

As has been seen in Chapter 2, theoretical calculations indicate that the bonding mechanism in TiS_2 is predominantly covalent. Also, it is expected that the number of free carriers is large enough to screen any long range Coulomb forces.

It is thus appropriate to describe the dynamics of the atomic vibrations within a short range valence force field (VFF) model. Given the limited number of experimental values to be fitted, it was decided to include only four parameters in the calculations. The VFF expression for the harmonic potential can then be written as (Lucovsky et al., 1976):

$$\Phi = \frac{1}{2} \sum_{S\text{-}Ti} k_r(\Delta r_{ij})^2 + \frac{1}{2} \sum_{S\text{-}Ag} k_s(\Delta r_{ij})^2$$
$$+\frac{1}{2} \sum_{S\text{-}Ti\text{-}S} k_\alpha(r\Delta\theta_{ijk})^2 + \frac{1}{2} \sum_{Ti\text{-}S\text{-}Ti} k_\beta(r\Delta\theta_{ijk})^2 \qquad (2)$$

where Δr_{ij} is the change in the S-Ti or S-Ag bond length and $\Delta\theta_{ijk}$ is the change in the considered bond angle.[1] The central force constant between the sulfurs and the titanium

---

[1] For a perfect octahedron, all the angles are 90^0. In TiS_2, the Ti-S-Ti angles are 90.8^0 while the S-Ti-S angles are either 89.2 or 90.8^0.

atoms is k_r while the one between the sulfur and silver atoms is k_s. k_α and k_β are non-central force constants arising from a deformation of the TiS_2 molecule.

The terms in the dynamical matrix corresponding to A-type vibrations can be evaluated in the following way. A set of N small displacements $\underline{\delta}^\ell$ along the N symmetry coordinates introduced in Section 3.7 is chosen (N is the number of A-type Raman active phonons in the considered configuration). The atomic positions can be written as:

$$\underline{r}_i' = \underline{r}_i + \underline{\delta}_i \tag{3}$$

with

$$\underline{\delta}_i = \sum_\ell \underline{\delta}_i^\ell \tag{4}$$

where $\underline{\delta}_i^\ell$ is the part of $\underline{\delta}^\ell$ corresponding to a motion of the atom i.

Under such displacements, the variation in a bond length is:

$$|\Delta r_{ij}| \simeq |(\underline{r}_i - \underline{r}_j)\cdot(\underline{\delta}_i - \underline{\delta}_j)| \tag{5}$$

while the variation in a bond angle is given by:

$$|r\Delta\theta_{ijk}| \simeq |(\underline{\delta}_i - \underline{\delta}_j)\cdot(\underline{r}_k - \underline{r}_j) + (\underline{\delta}_k - \underline{\delta}_j)\cdot(\underline{r}_i - \underline{r}_j)| \tag{6}$$

Using those expressions, it is possible to write the Hamiltonian as:

$$H = \frac{1}{2} \sum_{\ell} M^{\ell} (\delta^{\ell})^2 + \frac{1}{2} \sum_{\ell\ell'} \phi^{\ell\ell'} \delta^{\ell} \delta^{\ell'} \qquad (7)$$

so that the dynamical matrix is:

$$F^{\ell\ell'}(\underline{0}) = (M^{\ell} M^{\ell'})^{-\frac{1}{2}} \phi^{\ell\ell'} \qquad (8)$$

The predicted frequencies of the A-type modes are then given by the secular equation:

$$|[F] - [I]\omega^2| = 0 \qquad (9)$$

5.2- Frequency Calculations for $Ag_{1/3}TiS_2$

The fact that the silver atoms are mobile in the host structure at room temperature indicates that the silver is weakly coupled to the TiS_2 lattice. This is further evidenced by the small shift in energy of the E_g and A_{1g} phonons after intercalation. Therefore, the force constant k_s was assumed negligible unless it was actually necessary to give a non-zero frequency to some normal modes.

The frequencies of the A_{1g} and E_g modes can be obtained directly since their normal displacements are known (Lockwood, 1969). They are given by:

$$M_S\omega^2_{A_{1g}} = \frac{1}{2}(3k_r + k_s)\cos^2\theta + 12(2k_\alpha + k_\beta)\cos^2\theta \qquad (10)$$

$$M_S\omega^2_{E_g} = \frac{1}{2}(3k_r + k_s)\sin^2\theta + \frac{3}{2}(2k_\alpha + k_\beta)\sin^2\theta \qquad (11)$$

with θ, the z-Ti-S angle, equal to 55°20' (Wilson and Yoffe, 1969).

Those two equations suffice to determine the values of both $(k_r + k_s/3)$ and $(2k_\alpha + k_\beta)$.

The Hamiltonian for the C^2_{31} configuration, where the silver ions are ordered on octahedral sites, is:

$$\begin{aligned} H = {} & 3M_S(\dot{\delta}^1)^2 + 3M_S(\dot{\delta}^2)^2 + M_{Ti}(\dot{\delta}^3)^2 \\ & + \frac{9}{2}(\delta^1)^2(k_r + k_\alpha + k_\beta)\sin^2\theta \\ & + 6\delta^1\delta^3(-k_r + 2k_\alpha - k_\beta)\sin\theta\cos\theta \\ & + \frac{9}{2}(\delta^2)^2(k_r + 5k_\alpha + k_\beta)\sin^2\theta \\ & + 6(\delta^3)^2(k_r + 4k_\alpha + k_\beta)\cos^2\theta \end{aligned} \qquad (12)$$

It is to be noted that the δ^4 displacements have not been included since they correspond to the A_{1g} normal mode and hence do not couple to the other ones.

The Hamiltonian for the C^4_3 configuration, where the silver atoms are on the tetrahedral sites, is given by:

$$H = \frac{3}{2}M_S[(\dot{\delta}^1)^2 + (\dot{\delta}^2)^2 + (\dot{\delta}^3)^2] + \frac{3}{2}M_{Ti}[(\dot{\delta}^4)^2 + (\dot{\delta}^5)^2 + (\dot{\delta}^6)^2]$$

$$+ \frac{1}{2}M_S[[\dot{\delta}^7)^2 + (\dot{\delta}^8)^2 + (\dot{\delta}^9)^2] + \frac{1}{2}M_{Ag}(\dot{\delta}^{10})^2$$

$$+ \frac{9}{4}(\delta^1)^2(k_r + 6k_\alpha + k_\beta + k_s/2)\sin^2\theta + \frac{3}{4}\delta^1\delta^2\sqrt{3}k_s\sin^2\theta$$

$$- \frac{3}{2}\delta^1\delta^3k_s\sqrt{3}\sin^2\theta + \frac{9}{2}\delta^1\delta^4(-k_r + 2k_\alpha + 2k_\beta)\sin^2\theta$$

$$+ \frac{3}{2}\delta^1\delta^8k_\alpha\sqrt{3}\sin\theta\cos\theta - \frac{3}{2}\delta^1\delta^9k_s\sqrt{3}\sin\theta\cos\theta$$

$$+ \frac{3}{2}\delta^1\delta^{10}k_s\sqrt{3}\sin\theta\cos\theta + \frac{9}{4}(\delta^2)^2(k_r + 6k_\alpha + k_\beta + k_s/6)\sin^2\theta$$

$$- \frac{3}{2}\delta^2\delta^3k_s\sin\theta\cos\theta + \frac{9}{2}\delta^2\delta^5(k_r - 2k_\alpha - 2k_\beta)\sin^2\theta$$

$$+ 3\delta^2\delta^7k_\alpha\sin\theta\cos\theta - \frac{3}{2}\delta^2\delta^8k_\alpha\sin\theta\cos\theta - \frac{3}{2}\delta^2\delta^9k_\alpha\sin\theta\cos\theta$$

$$+ \frac{3}{2}\delta^2\delta^{10}k_s\sin\theta\cos\theta + \frac{9}{2}(\delta^3)^2(k_r + 6k_\alpha + 4k_\beta + k_s/3)\cos^2\theta$$

$$- 9\delta^3\delta^6(k_r + 4k_\alpha + 4k_\beta)\cos^2\theta - 6\delta^3\delta^7\cos^2\theta$$

$$- 6\delta^3\delta^8k_\alpha\cos^2\theta - 6\delta^3\delta^9k_\alpha\cos^2\theta - \frac{3}{2}\delta^3\delta^{10}k_s\cos^2\theta$$

$$+ \frac{9}{2}(\delta^4)^2(k_r + 4k_\alpha + \frac{5}{2}k_\beta)\sin^2\theta$$

$$+ \frac{3}{2}\delta^4\delta^8(-k_r + k_\alpha + 2k_\beta)\sqrt{3}\sin\theta\cos\theta$$

$$+ \frac{3}{2}\delta^4\delta^9(k_r - k_\alpha - 2k_\beta)\sqrt{3}\sin\theta\cos\theta$$

$$+ \frac{9}{2}(\delta^5)^2(k_r + 4k_\alpha + \frac{5}{2}k_\beta)\sin^2\theta + 3\delta^5\delta^7(k_r - 2k_\alpha - 2k_\beta)\sin\theta\cos\theta$$

$$+ \frac{3}{2}\delta^5\delta^8(-k_r + 2k_\alpha + 2k_\beta)\sin\theta\cos\theta$$

$$+ \frac{3}{2}\delta^5\delta^9(-k_r + 2k_\alpha + 2k_\beta)\sin\theta\cos\theta$$

$$+ 9(\delta^6)^2(k_r + 4k_\alpha + 4k_\beta)\cos^2\theta - 3\delta^6\delta^7(k_r + 4k_\alpha + 4k_\beta)\cos^2\theta$$

$$- 3\delta^6\delta^8(k_r + 4k_\alpha + 4k_\beta)\cos^2\theta - 3\delta^6\delta^9(k_r + 4k_\alpha + 4k_\beta)\cos^2\theta$$

$$+ \frac{3}{2}(\delta^7)^2(k_r + 4k_\alpha + 4k_\beta)\cos^2\theta + 3\delta^7\delta^8k_\alpha\cos^2\theta + 3\delta^7\delta^9k_\alpha\cos^2\theta$$

$$+ \frac{1}{2}(\delta^8)^2[3(k_r + 4k_\alpha + 4k_\beta)\cos^2\theta + k_s] + 3\delta^8\delta^9k_\alpha\cos^2\theta$$

$$+ \delta^8\delta^{10}k_s + \frac{3}{2}(\delta^9)^2(k_r + 4k_\alpha + 4k_\beta)\cos^2\theta + \frac{1}{2}(\delta^{10})^2 k_s \quad (13)$$

In this case, the force constant k_s has been included since it is essential to give a non-zero frequency to one of the modes involving silver atom motion.

The eigenvalues and eigenvectors of the dynamical matrices corresponding to the Hamiltonians (12) and (13) were evaluated for values of k_α between $-k_r$ and k_r. The values of $(k_r + k_s/3)$ and $(2k_\alpha + k_\beta)$ were obtained using the experimental values of the A_{1g} and E_g peaks observed from the $Ag_{0,33}TiS_2$ sample. The matrices were diagonalized on an IBM 370/148 computer using the standard program supplied in the IMSL library. The results for the regions in which the calculated frequencies are real are shown in Figures 5.1, 5.2 and 5.3.

It is to be noted that errors on the calculated curves coming from uncertainties in the frequencies of the A_{1g} and E_g modes are of the order of the width of the lines.

From Figure 5.1, one can see that the three extra Raman active A-type phonons predicted for the C_{3i}^2 configuration have frequencies quite similar to the observed values. Actually, with a value of $k_\alpha \simeq 0{,}25k_r$, the A_2 and A_3 peaks are fitted within 3% while the A_1 frequency is away from the predicted one by about 35% (128 cm^{-1} vs 175 cm^{-1}).

Regarding the C_3^4 configuration, Figure 5.2 indicates that, even though six of the predicted phonon frequencies are actually

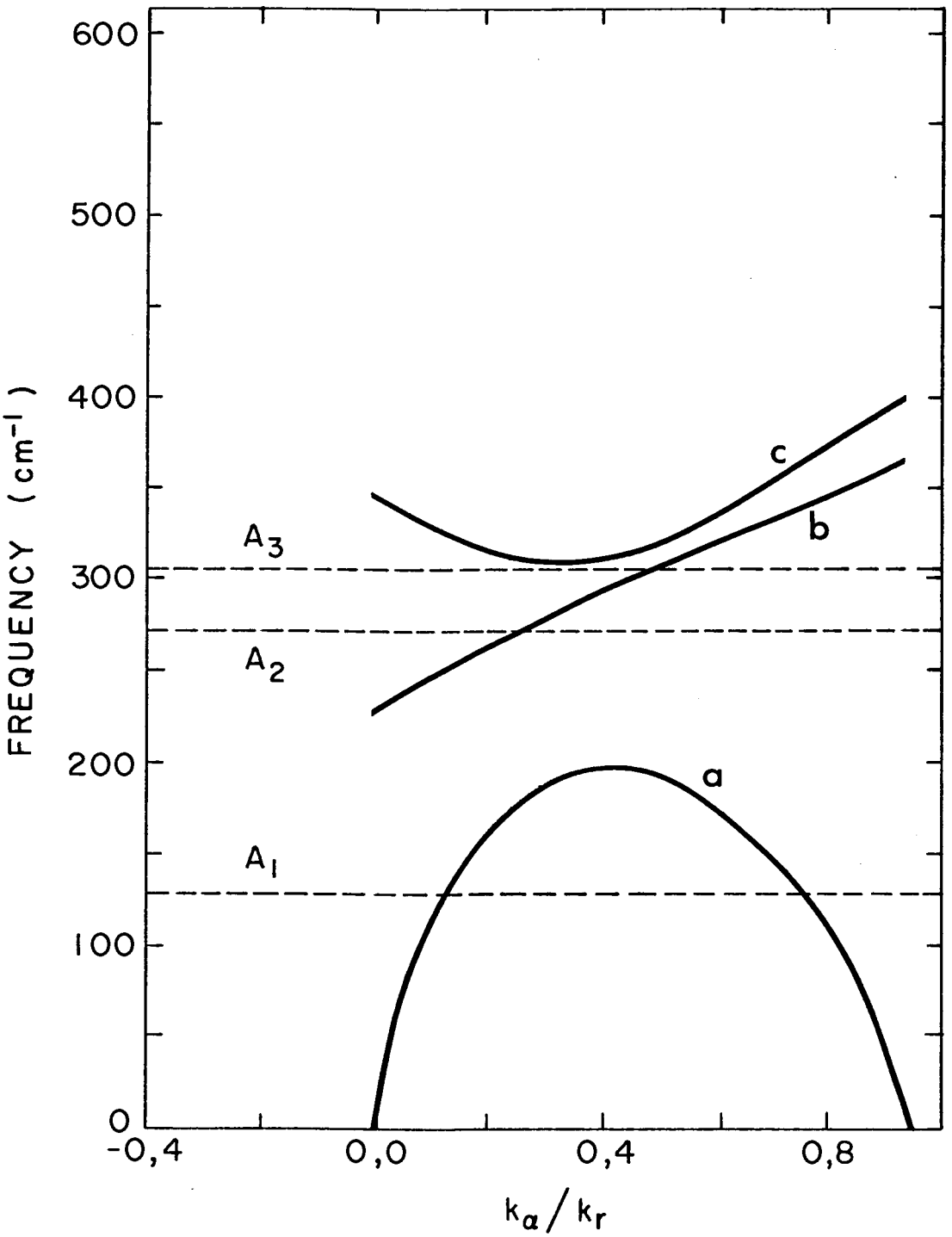

Figure 5.1- Frequency predictions for the folded-back A-type phonons in the C_{3i}^2 configuration as a function of k_α/k_r.

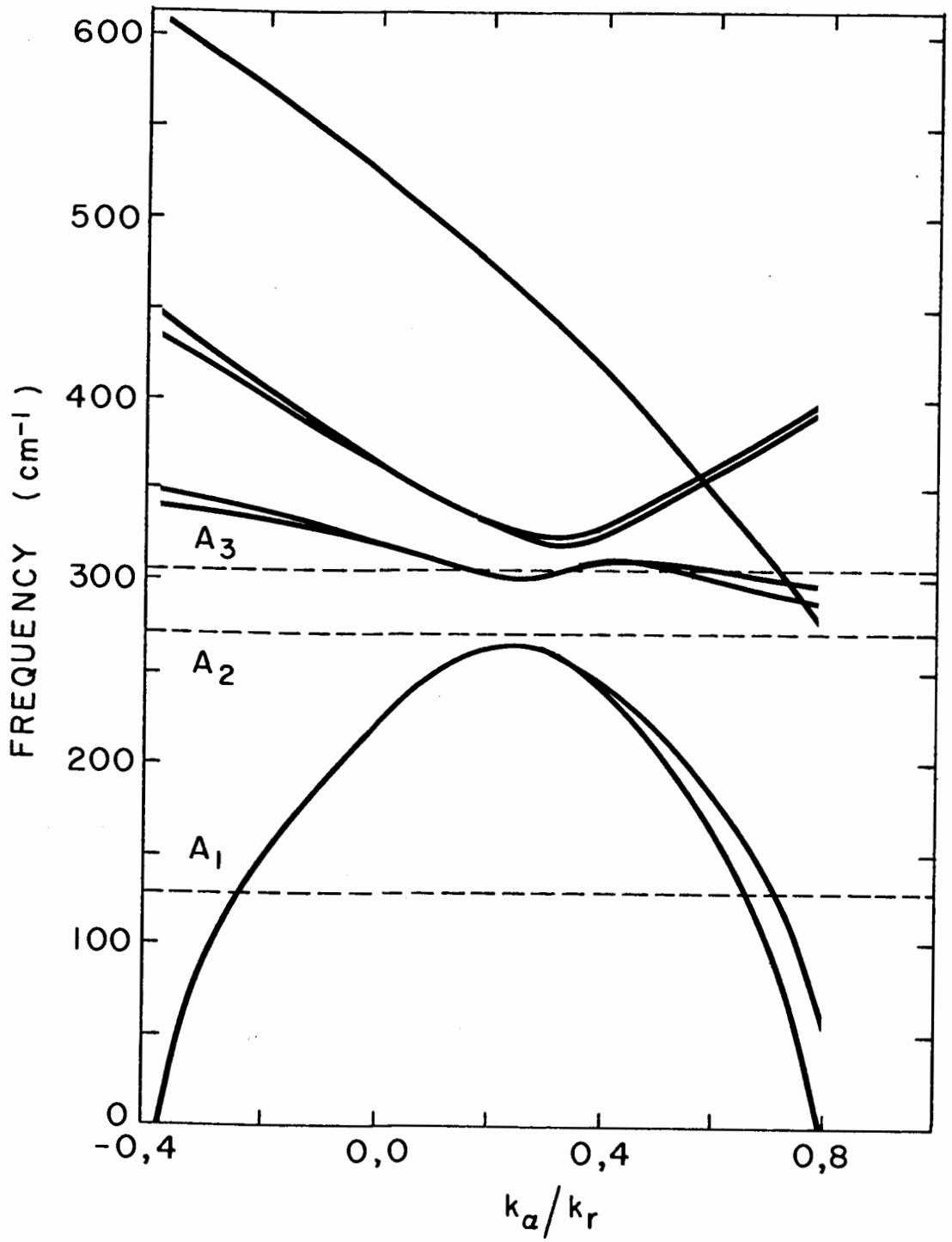

Figure 5.2- Frequency predictions for the folded-back A-type phonons in the C_3^4 configuration as a function of k_α/k_r and with $k_s = 0$.

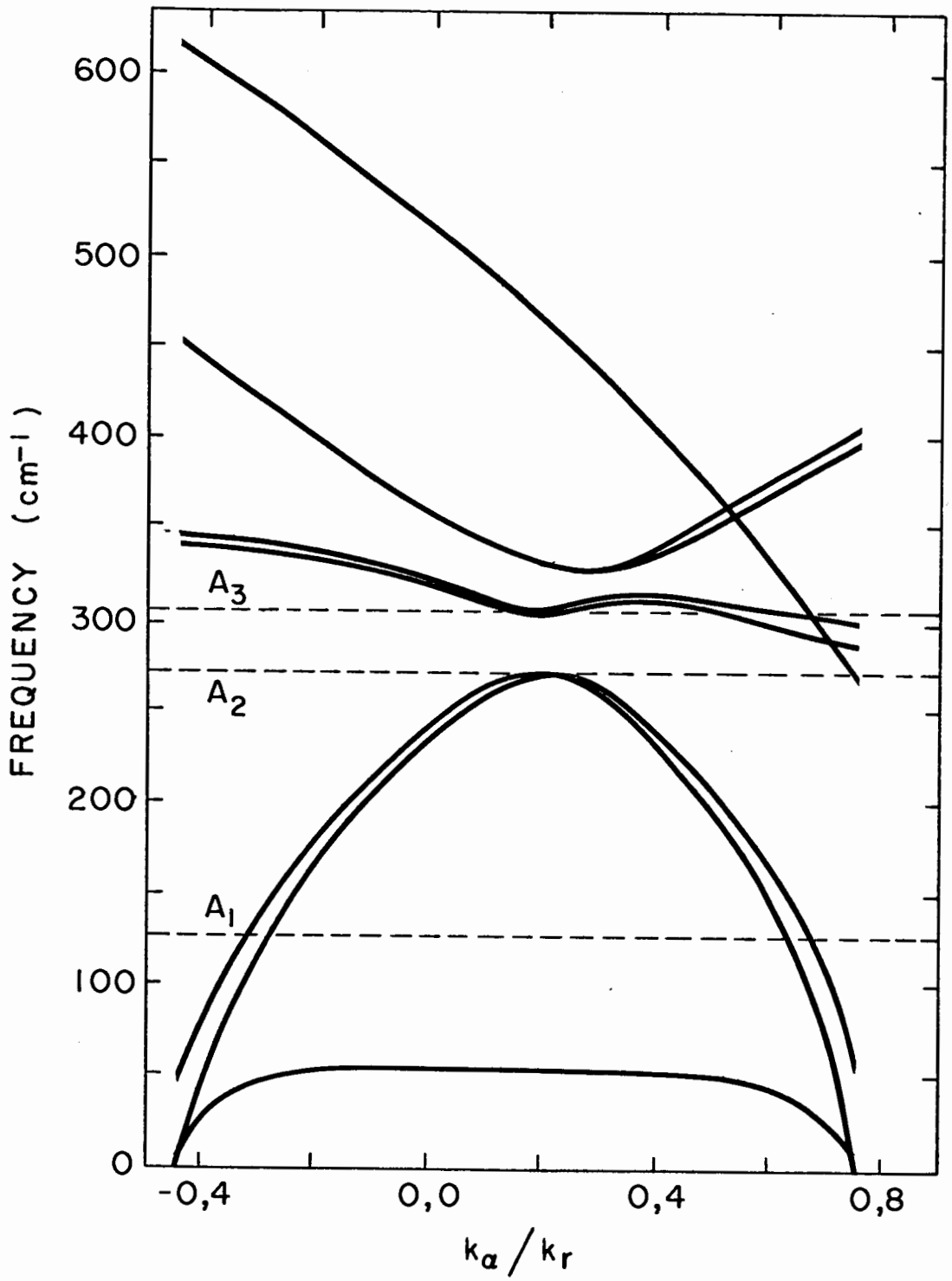

Figure 5.3- Frequency predictions for the folded-back A-type phonons in the C_3^4 configuration as a function of k_α/k_r and with $k_s = 0,20k_r$.

grouped in three near doublets and although two of those doublets fit very well the A_2 and A_3 frequencies, there is still two more phonons predicted but not observed and there are no phonons predicted in the vicinity of the A_1 peak.

Figure 5.3 shows the predictions for $k_s = 0{,}20k_r$. This value was considered an upper limit because the normal displacements corresponding to the A_{1g} mode were beginning to be significantly altered. The curves are very similar to the ones of Figure 5.2 except that the mode corresponding to silver motion has now a non-zero frequency. But that frequency is still less than half the one of the A_1 peak.

It is to be noted that in both Figures 5.2 and 5.3, there is a zero frequency mode corresponding to a translation of the full lattice. Also, the calculations leading to Figures 5.2 and 5.3 reproduced the frequency and normal displacements of the A_{1g} mode.

From all that precedes, it is concluded that the new peaks observed in the Raman spectra are consistent with the symmetry assignment and the frequency predictions of the VFF model if a C_{3i}^2 configuration is assumed. This strongly indicates that the silver ions occupy the vacant octahedral sites in the Van der Waals gap of the TiS_2 host and that a zone-folding mechanism takes place due to the ordering of the silver ions in a $\sqrt{3}a$ triangular superlattice.

The values of the force constants for which there is a best fit of the experimental values obtained from the x= 0,33 sample are then:

$$k_r \simeq 52 \text{ N/m} \tag{14}$$

$$k_\alpha \simeq 13 \text{ N/m} \tag{15}$$

$$k_\beta \simeq 18 \text{ N/m} \tag{16}$$

Figure 5.4 pictures the corresponding calculated normal displacements.

5.3- Monte Carlo Calculations: Theory

To obtain the behaviour of any parameter F(r) of the lattice gas described in Section 2.3, one has to evaluate, within a Boltzmann distribution, the following statistical average:

$$\langle F \rangle = \frac{\sum_r \exp(-E_r/kT) F(r)}{\sum_r \exp(-E_r/kT)} \tag{17}$$

where the sum extends over all the accessible states r of the system and E_r can be obtained from the Hamiltonian given by equation 2.9.

It is not possible to evaluate (17) explicitly but it is possible to obtain estimates of the average by Monte Carlo

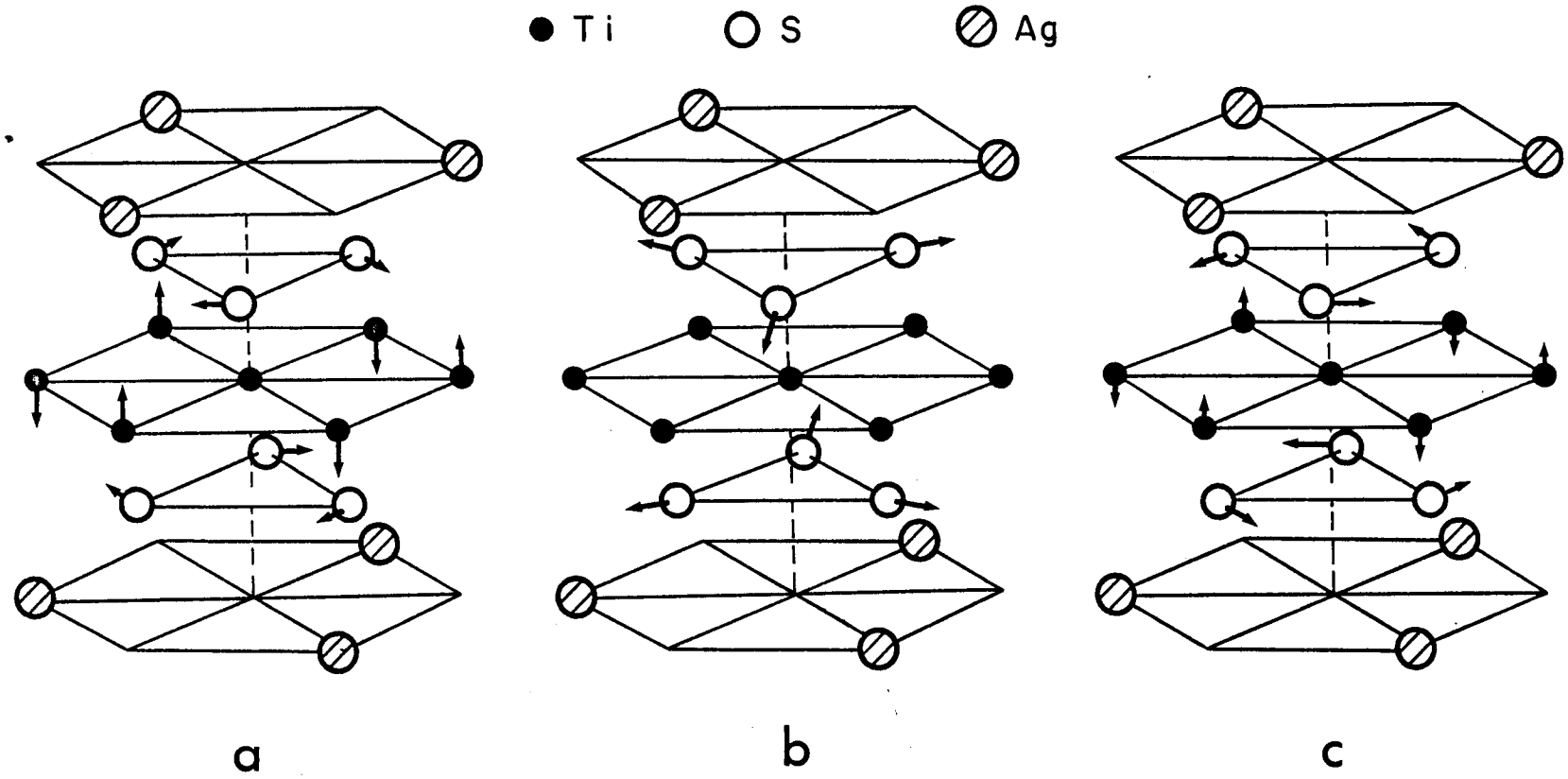

Figure 5.4- Normal mode displacements in $Ag_{1/3}TiS_2$. The letters a, b and c refer to the corresponding modes in Figure 5.1.

methods.[2]

This can be done by generating a certain number M of sample states r' on a finite lattice. The generation mechanism must be biased in such a way that it chooses a state r' according to the probability distribution:

$$p(r') = \frac{\exp(-E_{r'}/kT)}{\sum_{r'} \exp(-E_{r'}/kT)} \qquad (18)$$

An estimate for the average value of a parameter F(r') is then given according to:

$$\langle F \rangle = \frac{1}{M} \sum_{r'} F(r') \qquad (19)$$

For the calculations performed in this work, a petit ensemble distribution in which the number of particles is held constant was used instead of the grand ensemble distribution governed by a chemical potential. An algorithm for the sampling procedure is given in Table 5.1 while a more detailed description of the method can be found in Appendix C.

5.4- Monte Carlo Calculations: Results

The Monte Carlo calculations were performed on an IBM 370/155 computer using a triangular array of 30x30 sites. The initial configuration was an ordered one in which all the A sites were occupied and all the other sites empty (x= 1/3). The behaviour of the long-range order parameter η and the

[2]See for example Fosdick (1963) or Binder (1976)

TABLE 5.1

Chart flow diagram for the sampling procedure of the Monte Carlo calculations.

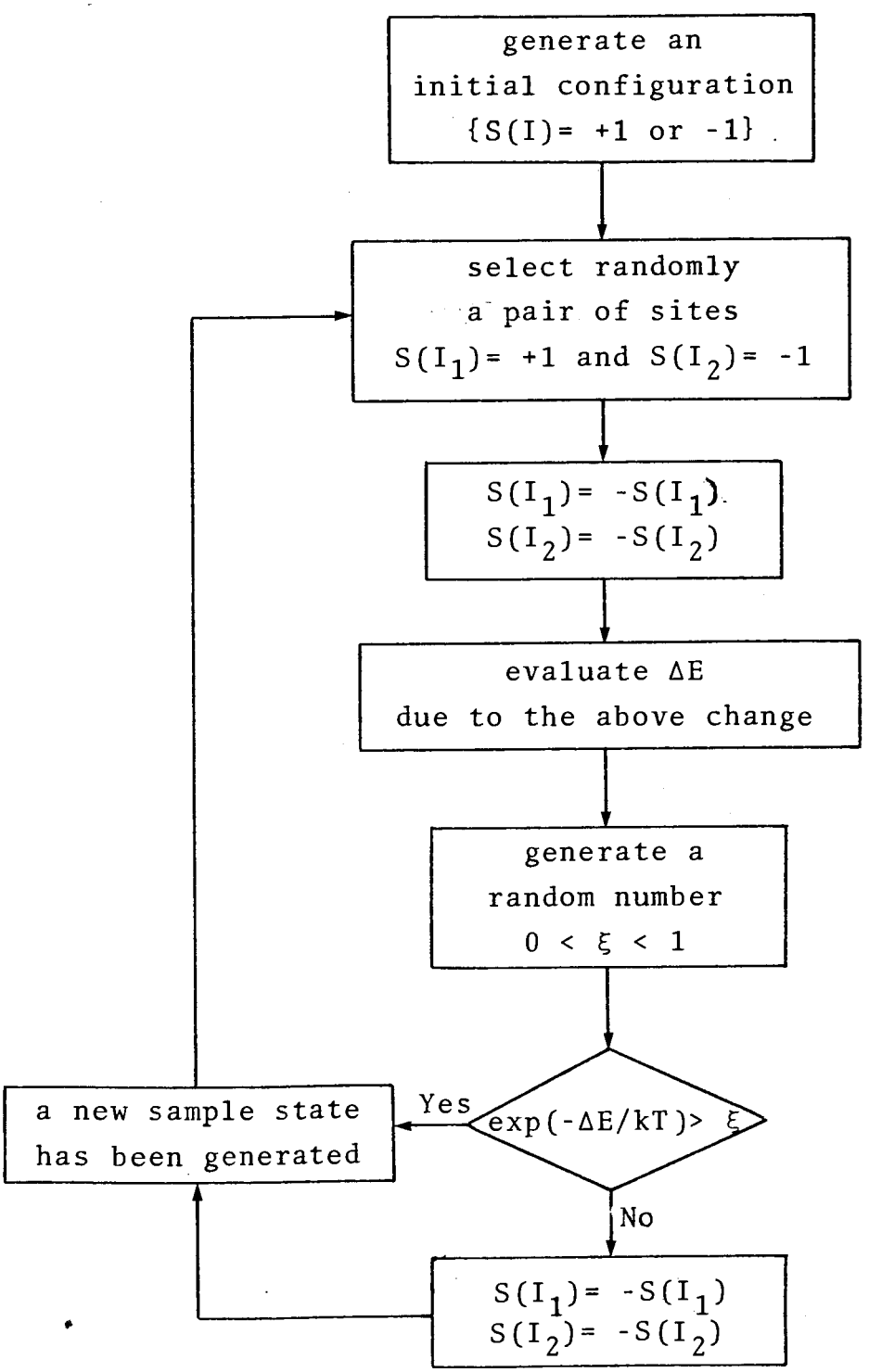

short-range order parameter ϕ was studied as a function of kT/U_1. ϕ was defined as the fraction of the occupied sites having only non-occupied sites as first neighbours.

The calculations reported here are with first neighbour interaction only. This is justifiable in view of the fact that screening is expected to take place so that U_2 and U_3 should be small compared to U_1. Also, tentative calculations have been performed with $U_2 = 0,1U_1$ and $U_3 = 0,05U_1$. Although the critical temperature was noticeably altered, the critical behaviour of the parameters evaluated appeared to be same.

The results of the calculations are shown in Figure 5.5 as a function of kT/U_1. The full and empty circles give respectively the value of η^2 and ϕ^2. The triangles reproduce the data points for the A_1 peak from the $Ag_{0,33}TiS_2$ sample given in Figure 4.11 with a value of $U_1 = 0,074$ eV chosen to match the critical point with the one given by the behaviour of η^2. Moreover, the three sets of points have been scaled so that they have a value of 1 at $kT/U_1 = 0,030$. Each Monte Carlo point represents the statistical average of the results of up to five different runs. It is not expected that the Monte Carlo calculations can yield the correct critical exponents but the obtained value of $kT/U_1 \simeq 0,35$ at the critical point agrees with the one given by the phase diagram of Figure 2.6.

The experimental values can be seen to agree well with an η^2 behaviour. This is a strong indication that the silver

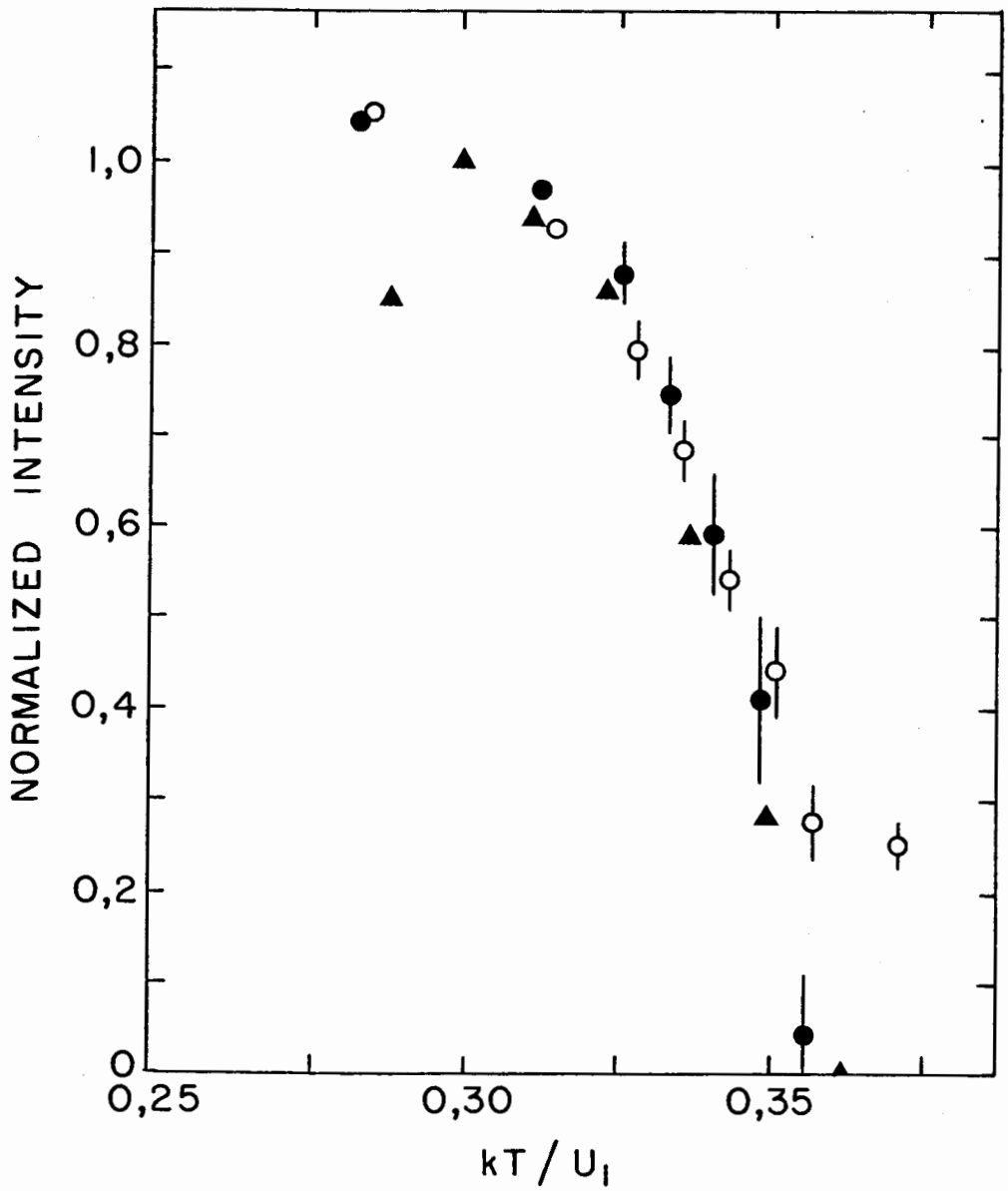

Figure 5.5- Monte Carlo predictions for the normalized intensity of a folded-back phonon. ● η^2; ○ ϕ^2; ▲ observed values for the A_1 peak in $Ag_{0,33}TiS_2$.

superlattice undergoes an order-disorder transition as expected from a lattice gas.

5.5- Comments on the Raman Spectra of $Ag_{0,19}TiS_2$

The Raman spectra obtained from the $Ag_{0,19}TiS_2$ sample are very similar to the ones obtained from the $Ag_{0,33}TiS_2$ sample, with approximately the same critical temperature. Moreover, electron diffraction patterns obtained from the x= 0,19 sample reveal the formation of a $\sqrt{3}a$ superlattice.

This is somewhat surprising since the phase diagram of Figure 2.6 rules out this possibility or at least implies a much smaller critical temperature. Moreover, recent calculations by Walker and Schick (1979) indicates that there should be a 2a triangular superlattice formed for $x \sim 0,20$.

One possible explanation would be that the crystal was not uniformly intercalated or that the silver ions cluster. But then, one should observe a superposition of the Raman spectra of pure TiS_2 and of $Ag_{1/3}TiS_2$. This means that the A_{1g} peak should be broadened or even split up into a doublet. But, as can be seen from Figures 4.6 and 4.7 and from Table 4.2, no such effect has been found.

A more likely explanation would be that there is staging in $Ag_{0,19}TiS_2$. Staging has been reported in several similar systems and in particular has been investigated by Raman scattering in intercalated graphite (Underhill et al, 1979). The irreducible

representations for the stage 2 $Ag_{1/6}TiS_2$ configuration have not been evaluated but one expects that the zone-folding mechanism would produce similar results to those observed in $Ag_{1/3}TiS_2$ because of the normally small phonon dispersion along the $\hat{k}_z$ direction.

VI. Concluding Remarks

Ag_xTiS_2 samples with $0 < x < 0,66$ have been prepared by electrointercalation. Samples with $x= 0,19$ and $x= 0,33$ have been examined with an electron microscope and it has been observed that at low enough temperatures the silver atoms order in a triangular array with a lattice spacing $a'= \sqrt{3}a$. Raman scattering experiments carried out on the same crystals have revealed that the ordering of the silver atoms gives rise to several additional peaks in the Raman spectra.

The frequency predictions from a simple valence field force model are in agreement with the observed values in $Ag_{0,33}TiS_2$ if it is assumed that the crystal point group changes from D^3_{3d} to C^2_{3i}. Such a change in the point group would be expected if the silver atoms were ordered in octahedral sites. The appearance of the additional spectral features in silver intercalated TiS_2 can therefore be attributed to a zone-folding mechanism.

This appears to be in contradiction with similar investigations performed on intercalated graphite. Although a zone-folding mechanism has been invoked to explain the Raman spectra of compounds of the type C_8X (Dresselhaus et al., 1977), experimental evidence from the C_8Cs system indicates that the extra features in the graphite spectra arise from disorder induced first-order Raman scattering from zone boundary modes

(Caswell and Solin, 1979). In particular, the new modes that appear in the Raman spectra are present both below and above the temperature of what is identified as a structural phase transition. But in C_8Cs, the Cs atoms are larger than the hexagonal net of C atoms in which they sit so that there are no empty sites available. As a result, the C_8Cs system cannot be represented by a lattice gas model and the exact nature of the structural phase transition is not well understood.

In $Ag_{0,33}TiS_2$ on the other hand, the temperature dependance of the Raman intensity of the additional peaks has been found to vary as the square of the long-range order parameter of a two-dimensional lattice gas and, above the transition temperature, the spectrum reduces to that of TiS_2. This η^2 behaviour is expected in the mean field approximation where short range interference effects are omitted. Obviously, there is a need for further calculations on the effect of disorder on the scattering intensity. These could include the effects of second and third neighbour interactions, a more rigorous analysis of the relation between the atomic motions and the ordering, and the effects of c-axis ordering.

More work will also be required to elucidate the many questions left unanswered in this thesis. For example, one can estimate the frequency of the oscillatory motion of the silver atoms in the following way. If one assumes that the silver-silver interaction potential can be represented by a cosine

function of amplitude $U_1/2$, then the Raman intensity should exhibit a resonance near the frequency (Dieterich and Peschel, 1977):

$$\omega_0 = \frac{2\pi}{1}\left(\frac{U_1}{2M_{Ag}}\right)^{\frac{1}{2}} \qquad (1)$$

where 1 is the periodicity of the potential. The value of $U_1 = 0{,}074$ eV has been found to provide the best fit of the Monte Carlo calculations to the Raman data, within a nearest neighbour approximation. With a value of $1 = \sqrt{3}a$, equation (1) would then predict a peak at roughly 10 cm^{-1}. A more careful examination of the Raman intensity at low frequency might be able to verify this prediction.

A complete structural study of Ag_xTiS_2 to verify the site attribution of the silver ions and to examine the hypothesis of staging would be appropriate. Also, no explanation for the peculiar characteristics of the A_1 peak with respect to the A_2 and A_3 peaks is provided. In particular, it is not understood why the A_1 peak half-width is somewhat smaller than the other ones and why its intensity increases with composition while the opposite appears to be true for the other A modes. A more detailed investigation of the behaviour of the Raman peaks as a function of temperature might yield answers to these questions and provide more information on the interaction of the intercalated specie with the host lattice.

It would be interesting to extend the investigations to other systems of the type M_xTiS_2 and in particular to the ones in which a 2a superlattice occurs. This would permit the development of a better model for the lattice dynamics of TiS_2 and eventually yield part of the phonon dispersion curves.

There is a rather large uncertainty inherent in the Raman intensity measurements. A more accurate evaluation of the critical temperature might be provided by an X-ray diffraction investigation. Moreover, this technique would hopefully give results much closer to T_c.

In summary however, it has been shown that silver intercalated TiS_2 is a good example of a lattice gas. This conclusion is warranted by the results of Raman scattering and electron diffraction experiments, and by the agreement between the Monte Carlo calculations and the experimental results. As a consequence, Ag_xTiS_2 and similar compounds should serve as excellent systems for more detailed studies on the physics of critical phenomena.

Appendix A- Irreducible Representations of the C_{3i} and C_3 Point Groups

The atoms of a primitive cell having the same surroundings are said to form an equivalent set. Let $\mathcal{G}_s$ be the site group of such an equivalent set of n atoms. Let γ refer to the representations of $\mathcal{G}_s$ and ζ refer to the representations of the crystal point group $\mathcal{G}_o(k)$. Then, the representations ζ compatible with the representations γ of the translations of the set of atoms s will correspond to lattice vibrations of the crystal (Fateley et al., 1972).

The site groups for each equivalent set of atoms can be found in International Tables for X-Ray Crystallography compatibility relations are established through the correlation tables as given in Fateley. In order to understand these tables, some definitions are in order.

Let t^γ be the number of translations in a site representation γ. The number of degrees of translational freedom from the corresponding set of atoms is then

$$f^\gamma = nt^\gamma \qquad (1)$$

Let a_ζ^γ be the number of degrees of freedom contributed by each species γ to a representation ζ of the point group and g_ζ be the degeneracy of that representation ζ. Then, one must have:

$$f^{\gamma} = \sum_{\zeta} a_{\zeta}^{\gamma} g_{\zeta} \qquad (2)$$

The irreducible representations for a given set of atoms can be constructed as follows:

$$\Gamma_s = \sum_{\zeta} a_{\zeta} \zeta \qquad (3)$$

where

$$a_{\zeta} = \sum_{\gamma} a_{\zeta}^{\gamma} \qquad (4)$$

The irreducible representations of the crystal are then formed by the direct sum of the irreducible representations of each equivalent set of atoms Γ_s.

The irreducible representations for $Ag_{1/3}TiS_2$ (C_{3i}^2) and $Ag_{1/3}TiS_2$ (C_3^4) are evaluated in Tables A.1 and A.2.

The representations corresponding to Raman active phonons can be identified according to the selection rules outlined in Section 3.4. Such an information is contained in the character tables of the different point groups.

Table A.3 gives the character tables of the C_{3i} and C_3 point group, as reproduced from Fateley et al. (1972).

TABLE A.1

Irreducible representations of the $Ag_{1/3}TiS_2$ crystal point group C_{3i}.

Site assignment	Site group
1 Ag in (0,0,1/2	C_{3i}
1 Ti in (0,0,0)	C_{3i}
2 Ti in $(0,0,z_1)$, $(0,0,z_1)$	C_3
6 S in (x,y,z_2), $(\bar{y},x-y,z_2)$, $(y-x,\bar{x},z_2)$ $(\bar{x},\bar{y},\bar{z}_2)$, $(y,y-x,\bar{z}_2)$, $(x-y,x,\bar{z}_2)$	C_1

Translations

C_{3i}: A_u (T_z), E_u (T_x,T_y)
C_3 : A (T_z), E (T_x,T_y)
C_1 : A (T_x,T_y,T_z)

Correlation

$$C_{3i} \longrightarrow C_{3i}$$

$$\Gamma_{Ag} = \Gamma_{Ti(C_3)} = A_u + E_u$$

f^γ	t^γ	$C_3 \longrightarrow C_{3i}$	g_ζ	$a_\zeta = a_A + a_E$
2	1	$A \longrightarrow A_g$	1	$1 = 1 + 0$
		$\longrightarrow A_u$	1	$1 = 1 + 0$
4	2	$E \longrightarrow E_g$	2	$1 = 0 + 1$
		$\longrightarrow E_u$	2	$1 = 0 + 1$

$$\Gamma_{Ti(C_3)} = A_g + A_u + E_g + E_u$$

TABLE A.1 (continued)

f^{γ}	t^{γ}	$C_1 \rightarrow C_{3i}$	g_{ζ}	a_{ζ}
18	3	$A \rightarrow A_g$	1	3
		$\rightarrow E_g$	2	3
		$\rightarrow A_u$	1	3
		$\rightarrow E_u$	2	3

$$\Gamma_S = 3A_g + 3A_u + 3E_g + 3E_u$$

$$\Gamma_{crystal} = 4A_g + 6A_u + 4E_g + 6E_u$$

TABLE A.2

Irreducible representations of the $Ag_{1/3}TiS_2$ crystal point group C_3.

Site assignment	Site group
1 Ag in $(0,0,z_1)$	C_3
1 S in $(0,0,0)$	C_3
1 S in $(0,0,z_2)$	C_3
1 S in $(0,0,\bar{z}_2)$	C_3
3 S in (x_3,y_3,z_3), $(\bar{y}_3,x_3-y_3,z_3)$, $(y_3-x_3,\bar{x}_3,z_3)$	C_1
3 Ti in (x_4,y_4,z_4), $(\bar{y}_4,x_4-y_4,z_4)$, $(y_4-x_4,\bar{x}_4,z_4)$	C_1

Translations

C_3: A (T_z), E (T_x,T_y)
C_1: a (T_x,T_y,T_z)

Correlations

$$C_3 \longrightarrow C_3$$

$$\Gamma_{Ag} = \Gamma_{S(C_3)} = A + E$$

f^γ	t^γ	$C_1 \longrightarrow C_3$	g_ζ	a_ζ
9	3	A $\longrightarrow$ A	1	3
		$\longrightarrow$ E	2	3

$$\Gamma_{S(C_1)} = \Gamma_{Ti} = 3A + 3E$$

$$\Gamma_{crystal} = 10A + 10E$$

TABLE A.3

Character tables for the C_{3i} and C_3 point groups.

C_{3i}	E	C_3	C_3^2	i	S_6^5	S_6	Raman active
A_g	1	1	1	1	1	1	Yes
E_g	1	ε	ε^*	1	ε	ε^*	Yes
	1	ε^*	ε	1	ε^*	ε	
A_u	1	1	1	-1	-1	-1	No
E_u	1	ε	ε^*	-1	$-\varepsilon$	$-\varepsilon^*$	No
	1	ε^*	ε	-1	$-\varepsilon^*$	$-\varepsilon$	

C_3	E	C_3	C_3^2	Raman active
A	1	1	1	Yes
E	1	ε	ε^*	Yes
	1	ε^*	ε	

$$\varepsilon = e^{i2\pi/3}$$

Appendix B- Symmetry Transformations for Cartesian Coordinates

Let $\{x_i\}$ be a set of 3s cartesian coordinates. One can see them as being a system of 3 coordinates **x**, **y** and **z** attached to each of the s atoms of the unit cell. A symmetry operation R can thus be separated in a part R^{pos} whose effect is to carry the atom k to a position k' and in a part R^{rot} which rotates the system of coordinates attached to the atom.

If one rewrites x_i as:

$$x_i = x_{\alpha k} \tag{1}$$

where k=1,...,s refers to the different positions and α refers to the three orientations in space, the symmetry transformations (2.39) can be written in the following way:

$$x_{\alpha k} \xrightarrow{R} (x_{\alpha k})' = \sum_{\beta} \sum_{k'} R^{pos}_{kk'} R^{rot}_{\alpha\beta} x_{\beta k'} \tag{2}$$

Tables B.1 and B.2 give the symmetry transformations (2) for the symmetry elements of the C_{3i} and C_3 point groups respectively. The transformations of the positions k k' are listed separately from the matrix elements $R^{rot}_{\alpha\beta}$. The position assigned to each atom of the unit cell is indicated in Figure 3.4.

One can then obtain a symmetry coordinate from each coordinate $x_{\alpha k}$ by forming the expression:

$$S^{\ell} = \sum_{R} (x_{\alpha k})' \tag{3}$$

TABLE B.1

Symmetry transformations for the elements of the point group C_{3i}.

Rotation matrices

$$E = \begin{pmatrix} 1 & 0 & 0 \\ 0 & 1 & 0 \\ 0 & 0 & 1 \end{pmatrix} \quad C_3 = \begin{pmatrix} -1/2 & 3/2 & 0 \\ -3/2 & -1/2 & 0 \\ 0 & 0 & 1 \end{pmatrix} \quad C_3^2 = \begin{pmatrix} -1/2 & -3/2 & 0 \\ 3/2 & -1/2 & 0 \\ 0 & 0 & 1 \end{pmatrix}$$

$$i = \begin{pmatrix} -1 & 0 & 0 \\ 0 & -1 & 0 \\ 0 & 0 & -1 \end{pmatrix} \quad S_6^5 = \begin{pmatrix} 1/2 & -\sqrt{3}/2 & 0 \\ \sqrt{3}/2 & 1/2 & 0 \\ 0 & 0 & 1 \end{pmatrix} \quad S_6 = \begin{pmatrix} 1/2 & \sqrt{3}/2 & 0 \\ -\sqrt{3}/2 & 1/2 & 0 \\ 0 & 0 & 1 \end{pmatrix}$$

Position transformations

Atom	Position	Operation					
	k \ k'	E	C_3	C_3^2	i	S_6^5	S_6
Ag	1	1	1	1	1	1	1
Ti(C_{3i})	2	2	2	2	2	2	2
Ti(C_3)	3	3	3	3	4	4	4
"	4	4	4	4	3	3	3
S	5	5	6	7	8	9	10
"	6	6	7	5	9	10	8
"	7	7	5	6	10	8	9
"	8	8	9	10	5	6	7
"	9	9	10	8	6	7	5
"	10	10	8	9	7	5	6

TABLE B.2

Symmetry transformations for the elements of the point group C_3.

Rotation matrices

$$E = \begin{pmatrix} 1 & 0 & 0 \\ 0 & 1 & 0 \\ 0 & 0 & 1 \end{pmatrix} \quad C_3 = \begin{pmatrix} -1/2 & \sqrt{3}/2 & 0 \\ -\sqrt{3}/2 & -1/2 & 0 \\ 0 & 0 & 1 \end{pmatrix} \quad C_3^2 = \begin{pmatrix} -1/2 & -\sqrt{3}/2 & 0 \\ \sqrt{3}/2 & -1/2 & 0 \\ 0 & 0 & 1 \end{pmatrix}$$

Position transformations

Atom	Position	Operation		
	k \ k'	E	C_3	C_3^2
Ag	1	1	1	1
S(C_3)	2	2	2	2
"	3	3	3	3
"	4	4	4	4
S(C_1)	5	5	6	7
"	6	6	7	5
"	7	7	5	6
Ti	8	8	9	10
"	9	9	10	8
"	10	10	8	9

In general, several different coordinates $x_{\alpha k}$ will yield the same symmetry coordinate S^{ℓ} through (3). The symmetry coordinates obtained from Tables B.1 and B.2 are given in Table 3.3.

Appendix C- Monte Carlo Program

The Monte Carlo program was written using Fortran IV. The calculations were performed on a lattice of 30x30 sites. A first array S(I) (I= 1 to 900) kept the actual state of site I (+1 or -1). A second one, N(I,J,K) (I= 1 to 900, J= 1 to 3, K= 1 to 6) contained the site number of the 18 first, second and third nearest neighbours of each site I, assuming a triangular lattice. The boundary conditions were such that the lattice was effectively folded in a torus, that is a site on a boundary had sites on the opposite boundary as neighbours. Two arrays, POS(I') and NEG(I") contained the site number of each sites in state +1 and -1 respectively. The initial configuration was one with all A sites in state +1 and all B and C sites in state -1.

In order to produce the sampling configurations, a pair of sites was randomly choosen, one site among the pool of numbers contained in POS and the other among NEG. The procedure described in Table 5.1 was then followed to decide if the states of these two sites should be exchanged.

A new configuration was considered to have been generated after the above test had been done on 1500 pairs. The parameters x_A, x_B, x_C and ϕ were then evaluated. The number M of different configurations generated varied from 1000 to 1300. The generation of between 300 and 800 states was required to allow the lattice to relax from its initial configuration. In order to be on the safe side, only the 500 last configurations were used

to evaluate the averages given by equation 5.19.

List of References

A. R. Beal, J. C. Knight and W. Y. Liang, J. Phys. C 5, 3531 (1972).

K. Binder, "Monte Carlo Investigations of Phase Transitions and Critical Phenomena", in Phase Transitions and Critical Phenomena, volume 5b, edited by C. Domb and M. S. Green, Academic Press, London (1976).

R. J. Birgeneau, H. J. Guggenheim and G. Shirane, Phys. Rev. B 8, 304 (1973).

F. W. Boswell, A. Prodon and J. M. Corbett, Phys. Stat. Sol. (a) 35, 591 (1976).

A. Bottini, M. Lazzari, G. Razzini, B. Rivolta, G. DeFelici, M. A. Voso and B. Scrosati, J. Electroanal. Chem. 96, 165 (1979).

G. Burns, F. H. Dacol, M. W. Schafer and R. Alben, Sol. St. Comm. 24, 753 (1977).

N. Caswell and S. A. Solin, Phys. Rev. B 20, 2551 (1979).

B. E. Conway, Theory and Principles of Electrode Processes, Ronald Press, New York (1965).

M. Danot, J. Bichon and J. Rouxel, Bull. Soc. Chim. Fr. 8, 3063 (1972).

W. Dieterich and I. Peschel, in Proc. Int. Conf. on Lattice Dynamics, edited by M. Balkanski, Flammarion, Paris, p. 524 (1977).

M. S. Dresselhaus, G. Dresselhaus, P. C. Eklund and D. D. L. Chung, Mat. Sci. Eng. 31, 141 (1977).

F. M. R. Engelsman, G. A. Wiegers, F. Jellinek and B. Van Laer, J. Sol. St. Chem. 6, 574 (1973).

Fast Ion Transport in Solids: Electrodes and Electrolytes, edited by P. Vashista, J. N. Mundy and G. K. Shenay, North-Holland, New York (1979).

L. D. Fosdick, J. Comp. Phys. 1, 245 (1963).

D. A. Gallagher and M. V. Klein, Phys. Rev. B 19, 4282 (1979).

D. L. Greenaway and R. Nitsche, J. Phys. Chem. Sol. 26, 1445 (1965).

K. Huang, Statistical Mechanics, Wiley, New York (1963).

International Tables for X-Ray Cristallography, Vol. I, edited by N. F. M. Henry and K. Lonsdale, Kynoch Press, Birmingham (1969)

A. Leblanc-Soreau, M. Danot, L. Trichet and J. Rouxel, Mat. Res. Bull. 9, 191 (1974).

N. LeNagard, O. Gorochov and G. Collin, Mat. Res. Bull. 10, 1287 (1975a).

N. LeNagard, G. Collin and O. Gorochov, Mat. Res. Bull. 10, 1279 (1975b).

D. J. Lockwood, in Proc. Int. Conf. on Light Scattering Spectra of Solids, edited by G. B. Wright, Springer-Verlag, New York, p. 75 (1969).

G. Lucovsky, J. C. Mikkelsen Jr., W. Y. Liang, R. M. White and R. M. Martin, Phys. Rev. B 14, 1663 (1976).

A. A. Maradudin, E. M. Montroll, G. H. Weiss and I. P. Ipatova, Theory of Lattice Dynamics in the Harmonic Approximation, second edition, Academic Press, New York (1971).

W. R. McKinnon and R. R. Haering, to be published in Sol. St. Ionics.

R. J. Nemanich, S. A. Solin and D. Guerard, Phys. Rev. B 16, 2965 (1977).

H. Poulet and J. P. Mathieu, Spectres de vibration et symétrie des cristaux, Gordon and Breach, Paris (1970).

A. Savitzky and M. J. E. Golay, Anal. Chem. 36, 1627 (1964).

M. Schick, F. S. Walker and M. Wortis, Phys. Rev. B 16, 2205 (1977).

J. E. Smith Jr., M. J. Nathan, M. W. Schafer and J. B. Torrance, in Proc. 11th Int. Conf. on the Physics of Semiconductors, Polish Scientific Publishers, Warsaw, p. 1306 (1972).

T. Takahashi and O. Yamada, J. Sol. St. Chem. 7, 25 (1972).

A. H. Thompson, K. R. Pisharody and R. F. Koehler Jr., Phys. Rev. Lett. 29, 163 (1972).

A. H. Thompson, Phys. Rev. Lett. 35, 1786 (1975).

A. H. Thompson, F. R. Gamble and C. R. Symon, Mat. Res. Bull. 10, 915 (1975).

M. Tinkham, Group Theory and Quantum Mechanics, McGraw Hill, New York (1964).

C. Underhill, S. Y. Leung, G. Dresselhaus and M. S. Dresselhaus, Sol. St. Comm. 29, 769 (1979).

W. K. Unger, J. M. Reyes, O. Singh, A. E. Curzon, J. C. Irwin and R. F. Frindt, Sol. St. Comm. 28, 109 (1978).

J. S. Walker and M. Schick, Phys. Rev. B 20, 2088 (1979).

M. S. Whittingham, Prog. Sol. St. Chem. 12, 41 (1978).

J. A. Wilson and A. D. Yoffe, Adv. Phys. 18, 193 (1969).

J. A. Wilson, Phys. Stat. Sol. (b) 86, 11 (1978).

R. W. G. Wyckoff, Crystal Structures, Interscience Publishers, New York (1965).

A. Zunger and A. F. Freeman, Phys. Rev. B 16, 906 (1977).